



LAWRENCE
LIVERMORE
NATIONAL
LABORATORY

LLNL-JRNL-551773

Kinematics and Dynamics of the East Pacific Rise Linked to Whole Mantle Convective Motions

D. B. Rowley, A. M. Forte, C. J. Rowan, S. P. Grand, N. A. Simmons

April 24, 2012

Science Advances

GEOLOGY

Kinematics and dynamics of the East Pacific Rise linked to a stable, deep-mantle upwelling

David B. Rowley,^{1*} Alessandro M. Forte,^{2,3} Christopher J. Rowan,^{1,4} Petar Glisović,² Robert Moucha,⁵ Stephen P. Grand,⁶ Nathan A. Simmons⁷

Earth's tectonic plates are generally considered to be driven largely by negative buoyancy associated with subduction of oceanic lithosphere. In this context, mid-ocean ridges (MORs) are passive plate boundaries whose divergence accommodates flow driven by subduction of oceanic slabs at trenches. We show that over the past 80 million years (My), the East Pacific Rise (EPR), Earth's dominant MOR, has been characterized by limited ridge-perpendicular migration and persistent, asymmetric ridge accretion that are anomalous relative to other MORs. We reconstruct the subduction-related buoyancy fluxes of plates on either side of the EPR. The general expectation is that greater slab pull should correlate with faster plate motion and faster spreading at the EPR. Moreover, asymmetry in slab pull on either side of the EPR should correlate with either ridge migration or enhanced plate velocity in the direction of greater slab pull. Based on our analysis, none of the expected correlations are evident. This implies that other forces significantly contribute to EPR behavior. We explain these observations using mantle flow calculations based on globally integrated buoyancy distributions that require core-mantle boundary heat flux of up to 20 TW. The time-dependent mantle flow predictions yield a long-lived deep-seated upwelling that has its highest radial velocity under the EPR and is inferred to control its observed kinematics. The mantle-wide upwelling beneath the EPR drives horizontal components of asthenospheric flows beneath the plates that are similarly asymmetric but faster than the overlying surface plates, thereby contributing to plate motions through viscous tractions in the Pacific region.

INTRODUCTION

Slab pull and ridge push (1) are almost universally regarded as the principal driving forces of plate tectonics. Secondary force contributions include various resistive forces, such as deviatoric stresses associated with slabs sinking through the viscous mantle (1–4), drag at the bottom of the plates, friction along plate-bounding faults, and bending of plates at subduction zones (5, 6). In this parameterized representation of plate driving forces, the force due to descending lithospheric slabs (slab pull) is found to be about an order of magnitude stronger than other forces (1, 3, 7), a view that has predominated over the past four decades (8).

Plate tectonics is thus conceived as a top-down, plate-driven convective system (9–11), where the plates themselves provide the buoyancy forces that drive their surface motion and deeper convective flow in the mantle. Top-down convection is justified when the dominant buoyancy sources are controlled by mantle cooling from above and internal heating of the mantle due to secular cooling and radioactive decay (12). Previous estimates of the core-mantle boundary (CMB) heat flux of ≤ 4 TW (13–15) are less than 10% of the total top of mantle heat flux of 39 ± 3 TW (12). This low heat flux across the CMB precludes the development of a strong lower thermal boundary layer necessary to generate significant deep buoyancy forces associated with active hot upwelling (15). Therefore, active mantle flow driven by heating at the base of the mantle has been largely dismissed as a driver of surface tectonic processes (8).

However, more recent estimates of the CMB heat flux range from 14 to 20 TW (16, 17), as much as 50% of the total heat flux at the top of the mantle. These more recent estimates are in line with mantle dynamic estimates of the global buoyancy fluxes (8), which imply that up to a half of the buoyancy flux driving plate motions may derive from the deep mantle and the other half from slab buoyancy, with lesser contributions from ridge push and other traditionally identified plate drivers.

Here, we focus on the behavior of mid-ocean ridges relative to the deep mantle, and specifically the anomalous kinematic behavior of the East Pacific Rise (EPR). We further highlight the absence of correlated subduction-related buoyancy fluxes of the Pacific and Farallon plates on either side of the EPR that might otherwise account for the observed anomalous behavior of the EPR. When combined with insights from joint seismic-geodynamic tomography-based modeling of mantle flow, these observations provide strong support for significant deep-mantle contributions to plate dynamics in the Pacific hemisphere.

RESULTS

Mid-ocean ridges, ridge residence times, and the EPR

In the top-down, plate-driven mantle flow regime (9), the dominance of slab pull implies that mid-ocean ridges, the sites of plate divergence, are passive features, with ridge axes free to migrate over the mantle as dictated by the vagaries of changes in the balance of slab-pull and ridge-push forces resolved along each ridge segment. Mantle upwelling and decompression melting at ridges are similarly viewed as passive, localized responses to plate divergence driven by far-field, subduction-driven flow.

If spreading ridges are truly passive, then mid-ocean ridge axes would be expected to migrate relative to the deep mantle. In the following discussion, we distinguish between ridge-parallel and ridge-perpendicular directions of ridge migration. Ridge-parallel migration is controlled solely by plate motions in the deep-mantle frame of reference

2016 © The Authors,
some rights reserved;
exclusive licensee
American Association
for the Advancement
of Science. Distributed
under a Creative
Commons Attribution
NonCommercial
License 4.0 (CC BY-NC).

¹Department of the Geophysical Sciences, University of Chicago, 5734 South Ellis Avenue, Chicago, IL 60637, USA. ²GEOTOP, Université du Québec à Montréal, Montréal, Québec H3C 3P8, Canada. ³Department of Geological Sciences, University of Florida, Gainesville, FL 32611, USA. ⁴Department of Geology, Kent State University, 221 McGilvrey Hall, Kent, OH 44242, USA. ⁵Department of Earth Sciences, Syracuse University, Syracuse, NY 13244, USA. ⁶Jackson School of Geosciences, University of Texas at Austin, Austin, TX 78712, USA. ⁷Atmospheric, Earth, and Energy Division, Lawrence Livermore National Laboratory, Livermore, CA 94551, USA.
*Corresponding author. Email: drowley@uchicago.edu

(defined below), and we will return to this component later in the discussion. In contrast to this, and the main focus of discussion here, is ridge-perpendicular migration. The rate of ridge-perpendicular motion as a function of time reflects a combination of half-spreading rate, asymmetry in accretion, and absolute plate motions in a deep-mantle frame of reference (18). In turn, the spreading rate and absolute plate motion should be controlled by the subduction-related buoyancy fluxes of the diverging plates. Any asymmetry in subduction-related buoyancy fluxes should result in ridge-perpendicular migration in the direction of the more negatively buoyant plate, with the rate of ridge migration increasing with increasing subduction-related negative buoyancy. We explore ridge migration behavior by computing the ridge residence time (RRT) for all main ocean basin spreading systems over the past 83 My (Fig. 1). We define RRT as the amount of time a spreading axis has occupied any given 0.5° by 0.5° grid cell, as determined by rotating the present-day oceanic age grid (19) at 1-My time steps from 0 to 83 million years ago (Ma) [C34ny (20)]. The location of ridges at each time step is demarcated by grid cells, where the age of the oceanic lithosphere equals the reconstruction age to within 1 My. For much of this analysis, we define the deep-mantle frame of reference as the “fixed” Indo-Atlantic hot spot frame, based on the rotation parameters of Nubia relative to the Indo-Atlantic hot spots (see table S1) (21). Figure 2 demonstrates that the RRT pattern is effectively the same, although slightly shifted spatially, when computed in the fixed Pacific hot spot frame of reference (22). Figure S1 reconstructs the RRTs in

the no-net-rotation (NNR) frame of reference back to 50 Ma and again shows long EPR residence times (see the Supplementary Materials). These comparisons indicate that our conclusions are not dependent on the particular choice of reference frame.

Late Cretaceous and Cenozoic finite plate rotations were compiled for each plate pair in the global ridge system from the data sources summarized in fig. S2 and listed in full in table S1 (see the Supplementary Materials). Where possible, finite rotation parameters with estimated uncertainties in the form of covariance matrices (23) are used, and the fit of synthetic flow lines to the trend of fracture zones in gravity data was assessed as a first-order check on reconstruction quality. Absolute ages for all rotations were assigned according to the CK95 time scale (20).

On symmetrically spreading ridges, the motion of the ridge axis relative to the separating plates is given by the half-spreading rotation. Motion of the asymmetrically spreading EPR axis is given a spreading rotation scaled to the estimated Pacific spreading fraction during each interval (24). Figure 3 shows reconstructed EPR positions in the Indo-Atlantic hot spot frame of reference at 5-My time steps, with their associated uncertainties (table S2), based on different plate circuits.

The plate circuit most commonly used to link the Pacific to the rest of the global plate system, and the Indo-Atlantic hot spot frame, goes through Antarctica via the Pacific-Antarctic Ridge (Fig. 3A). Reconstructions without any motion between West and East Antarctica produce a significant misfit of the geology of New Zealand across the

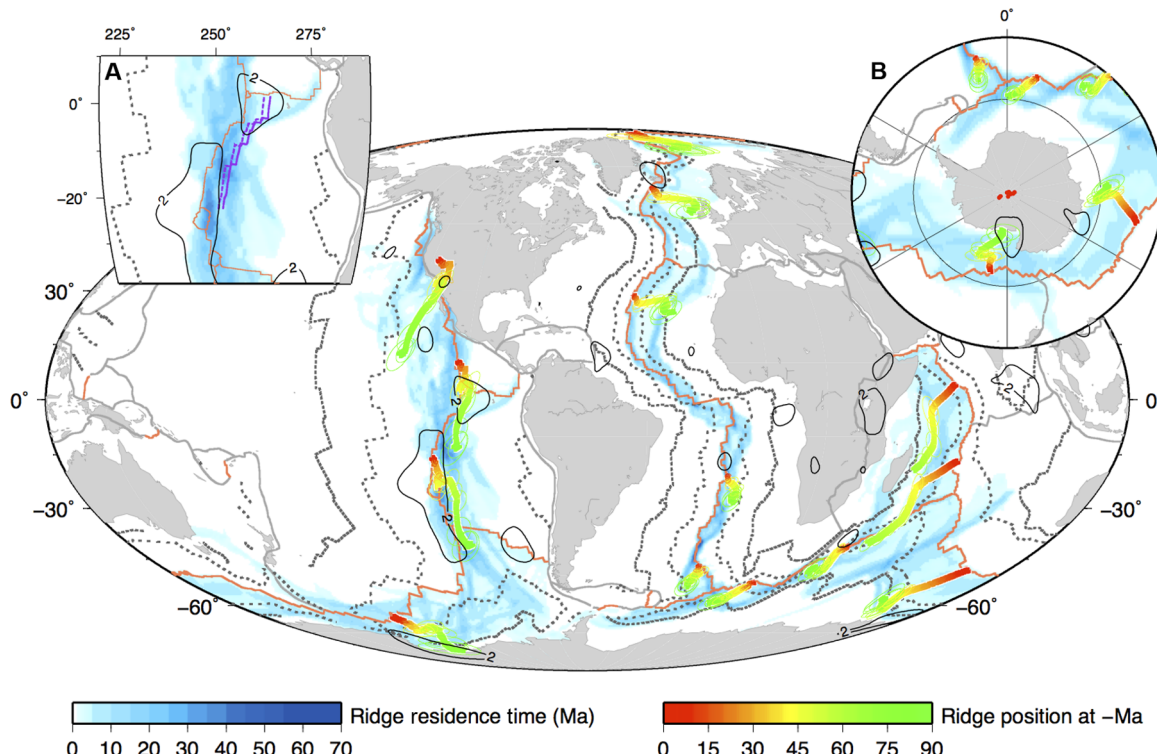


Fig. 1. RRTs and ridge axis migration relative to the fixed Indo-Atlantic reference frame with detailed inset (A) of the EPR. RRTs and ridge axis migration relative to the Indo-Atlantic hot spot frame of O’Neill *et al.* (21). Unshaded regions are for RRTs <1 My. Gray dotted lines are 33.5 Ma (C13no), and solid gray lines are 83 Ma (C34ny) isochrons from the age grid (19). The asymmetric distribution of the 33.5-Ma isochrons relative to the EPR on the Nazca and Pacific plates is illustrated. Red lines are modern-day plate boundaries (75). Contour encloses regions with upwelling velocities of >2 cm/year at 650 km. (A) Top left inset map shows details of the RRTs along the EPR, with modeled radial flow velocity contour of 2 cm/year at 650-km depth. The predicted positions of the EPR were spreading to have been persistently symmetric over 50 Ma and 80 Ma, and are shown by the two isochrons. (B) South polar view of the same data. Red dots show the reconstructed positions of the present-day south pole ($\sim 90^\circ$) in the Indo-Atlantic frame of reference in 10-My intervals back to 80 Ma, demonstrating that it has drifted less than 5° latitudinally and hence has been essentially fixed in this frame of reference for the past 80 My.

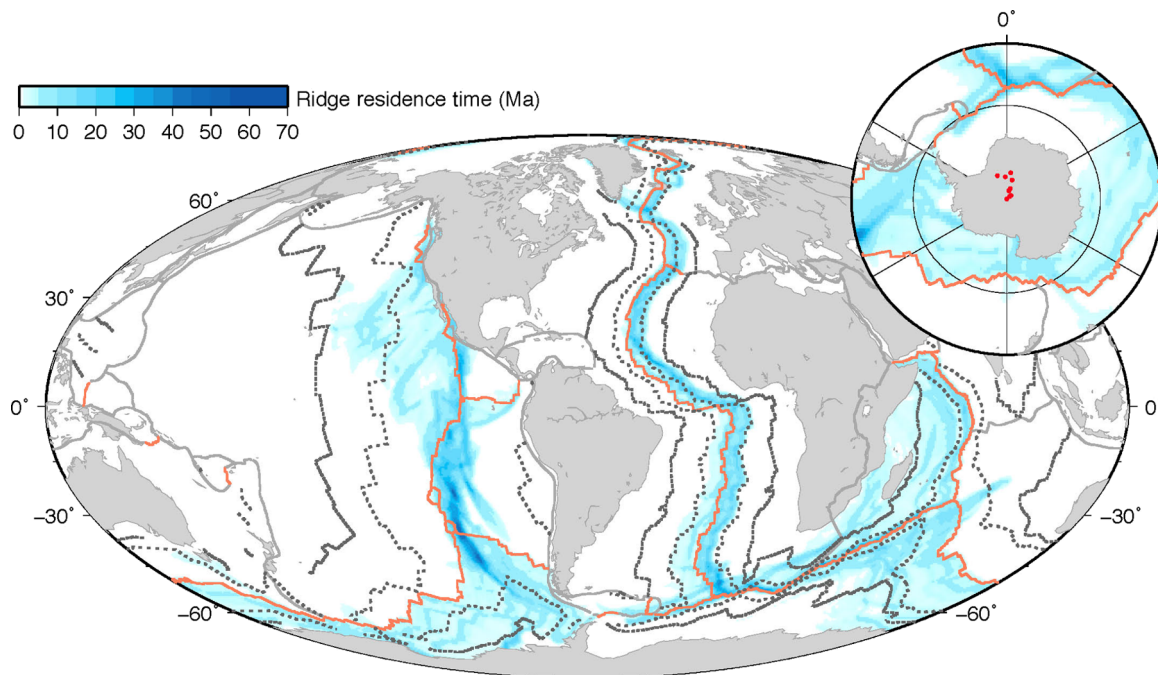


Fig. 2. RRTs and ridge axis migration relative to the fixed Pacific hot spot reference frame (22). (Inset) South polar view (same as in Fig. 1B).

Alpine Fault. This misfit arises because the Campbell Plateau and most of South Island New Zealand are kinematically linked to West Antarctica through the Southwest Pacific Ridge, whereas regions west of the Alpine Fault are linked to East Antarctica through the Southeast Indian Rise. We use published rotations between East and West Antarctica from C18no and C8no (25). Earlier deformation, possibly starting as early as the Late Cretaceous, has been proposed (26), but direct geological evidence from within Antarctica remains elusive; this highlights the fact that it is more difficult to quantify errors for rotations across plate boundaries lacking discrete identifiable conjugate points, most often magnetic reversal picks and ridge-transform intersections. This is also the case for the East African Rift, but in this case, the total estimated finite rotation between Somalia and Nubia since 25 Ma is small ($\leq 1^\circ$) and thus should not contribute significant additional uncertainty.

An alternative plate circuit that circumvents West Antarctica by rotating through East Antarctica from the Pacific via the Australian plate has been suggested (Fig. 2B) (27). The Pacific-Australian plate boundary has been transpressional since C11.2no (30.1 Ma), but finite rotations in this period can be calculated by closing the Macquarie triple junction using rotations from the Pacific-Antarctic Ridge (28) and the Southeast Indian Rise (29). Before C11.2no, Eocene-Oligocene oceanic spreading in the Emerald Basin (30) back to initial opening at approximately 52 Ma and Cretaceous-Eocene oceanic spreading in the Tasman Basin (31) allow finite rotations for this boundary to be directly determined, assuming that there was no significant deformation between the Lord Howe Rise and the Campbell Plateau/Pacific plate between the cessation of Tasman Basin spreading and the initiation of Emerald Basin spreading. The Campbell Plateau has been attached to the Pacific plate for at least the past 83 My (32). The advantage of using the circuit through Lord Howe Rise is that motion between the Pacific and Australian plates is directly constrained by magnetic

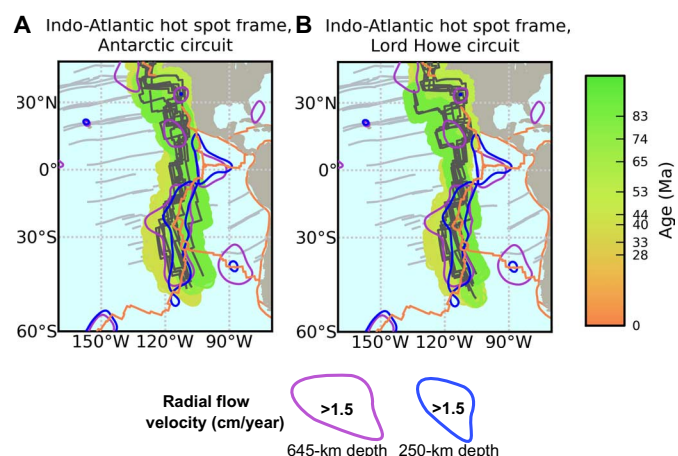


Fig. 3. Reconstruction of Pacific isochrons and associated uncertainties using various plate circuits and in the Pacific hot spot frame of reference. (A) Reconstructions using the more traditional Pacific-West Antarctica-East Antarctica plate circuit. **(B)** Our preferred reconstruction of EPR migration since 83 Ma along a plate circuit using constraints from the Emerald Basin (30) and assuming no earlier motion between the Campbell Plateau and Lord Howe Rise. Contours of modeled radial flow velocity in the underlying mantle are overlaid to show the spatial relationship between paleogeographic stability of the EPR axis and locus of mantle upwelling.

anomaly and fracture zone data, with explicit rotation uncertainties, for the entire period covered by our reconstructions. For this reason, our preferred reconstruction of EPR motion uses this circuit to tie the Pacific plate to the global plate system. However, as Fig. 3 demonstrates, the reconstructed position of the EPR in the Indo-Atlantic hot spot frame over the past 83 My shows similar longitudinal stability using

both the traditional Pacific–West Antarctica–East Antarctica–Africa circuit (Fig. 3A) and our preferred Pacific–Australia–East Antarctica–Africa circuit (Fig. 3B).

Antarctica has been effectively stationary with respect to latitude over the past 83 My on the basis of the fixed Indo-Atlantic hot spot frame of reference (Fig. 1B) (21), requiring circum-Antarctic ridges to migrate away from Antarctica at approximately their respective half-spreading rates. The faster-spreading Australian-Antarctic and Southwest Pacific ridges have moved more rapidly over the mantle, resulting in shorter RRTs (usually <20 My), whereas the slow-spreading Southwest Indian Ridge has migrated slowly, leading to RRTs in excess of 30 My. Africa is also moving slowly in this frame of reference; the fast-spreading Carlsberg and Central Indian ridges have thus rapidly migrated northeast since 83 Ma, resulting in shorter RRTs (Fig. 1A). Overall, this pattern of ridge migration conforms to the expected passive behavior in a largely plate-driven convective system and has often been used to justify this view.

The longest RRTs are associated with two ridge systems: the Mid-Atlantic Ridge (MAR) in the South and (to a lesser degree) the Central Atlantic and the EPR. The southern MAR has subsegments with the longest RRTs (up to 69 My) of all the ridges analyzed. Tristan da Cunha (33) is perhaps the most important member of the Indo-Atlantic constellation of hot spots used to determine motions in this frame of reference and is thus fixed by definition in these reconstructions. Before ~20 Ma, Tristan da Cunha was coincident with the MAR, requiring the southern MAR to remain essentially fixed. Subsequent to ~20 Ma, the MAR has slowly migrated westward relative to Tristan da Cunha. Together, these result in the long RRTs. Farther north, in the equatorial and central Atlantic, Fig. 1A shows two phases where the MAR remained relatively fixed at least longitudinally, first from about 80 Ma to 50 Ma and then from about 40 Ma to present. Once again, these long RRTs can be attributed to relatively slow spreading in the central Atlantic, with the length weighted mean half-spreading rate of about 15 km/My, which is close to the rate of migration of Africa relative to the Indo-Atlantic hot spot frame of reference during these two intervals (21).

The EPR is also characterized by long residence times (up to 45 My) but, in contrast to the MAR, is not similarly constrained to move slowly in the Indo-Atlantic, Pacific, or NNR frames of reference. The EPR has been characterized by consistently fast half-spreading rates that, to date, locally exceed 72.5 km/My (34). Over the past ~50 My, the length weighted mean EPR half-spreading rate has exceeded 60 km/My (24). These high divergence rates imply that, for most possible motions of the Pacific and Farallon/Vancouver/Nazca/Cocos plates, the EPR would be expected to migrate rapidly in a ridge-perpendicular direction across the mantle.

Figure 4 compares the integrated ridge-perpendicular component of ridge migration over the past 80 My to the cumulative amount of oceanic spreading for each of the major mid-ocean ridge segments in the current plate system. This figure illustrates that the extremely low ratio of lateral ridge migration to total spreading is a unique feature of the EPR. In other ridge systems, higher spreading rates correlate with more rapid lateral migration (for example, Central Indian and Carlsberg Ridges). Note that since 40 Ma (large blue squares in Fig. 4), the cumulative ridge-perpendicular motion of the EPR was ~0 km, for an associated ~6600 km of spreading. For times earlier than this, the remaining uncertainties in the correct rotations connecting through New Zealand and/or between East and West Antarctica may account for the larger estimates of ridge-perpendicular motions of the EPR in

the Indo-Atlantic reference frame. In addition, the clockwise reconfiguration of EPR geometry following C7ny (~24.7 Ma) [see Fig. 1 of Rowan and Rowley (24)] results in a present-day great-circle geometry (Fig. 3) that increases estimated ridge-perpendicular migration of older ages.

Reconstruction of the position of each plate relative to any other plate or the Indo-Atlantic reference frame involves uncertainties in the rotation parameters used to determine their reconstructed positions (35). Figure 1 shows the reconstructed positions back to 83 Ma of specific points corresponding to each major ridge axis as a function of time with associated uncertainty ellipses plotted every 5 My. The ellipses represent the combined 95% confidences from summing all the rotations in the plate circuit linking the Pacific plate to the Indo-Atlantic hot spot reference frame, with the largest contribution to these uncertainties coming from the rotation of Nubia relative to the fixed Indo-Atlantic hot spots (21). The RRTs in Figs. 1 and 2 do not incorporate these uncertainties, allowing for the possibility that the EPR axis may have resided above the same regions of the deep mantle for most of the 83 My covered by our reconstructions.

The EPR is also characterized by highly asymmetric spreading over at least the last 51 My (to chron C23ny), where magnetic reversal data on both the Nazca and Pacific plates explicitly constrain this quantity (24). On average, between 55 and 60% of oceanic lithosphere has been added to the Nazca plate and only 40 to 45% to the Pacific plate (24). These estimates incorporate the combined effects of asymmetric spreading and asymmetric ridge jumping (see asymmetry in the 33.5-Ma isochrons in Fig. 1), where ridges preferentially jump westward on the Pacific plate, or ridge propagators on the western sides of overlapping ridge segments preferentially persist relative to those along the eastern sides. This results in considerable variability of asymmetric accretion among different segments of the EPR, both in amount and as a function of time (19, 24, 36). Before ~51 Ma, asymmetric spreading is not directly observable because of subduction of older Nazca plate beneath South America.

Persistent asymmetric spreading and ridge jumping have had direct impacts on ridge-perpendicular migration of the EPR. If spreading had been symmetric in the past 50 My, then the EPR would presently be more than 500 km east of its current position (Fig. 1A). The lateral migration of the EPR would have increased to greater than 650 km if asymmetric accretion has persisted over the past 80 My (Fig. 1A). This suggests that asymmetric spreading and asymmetric ridge jumping have not been random but have served to systematically maintain the EPR over the same region of the mantle.

The previous analysis emphasizes the ridge-perpendicular component of motion of the EPR. As shown in Figs. 1 and 2, there is a significant component of ridge-parallel motion. This aspect of the motion is readily understood as a direct kinematic consequence of the essentially fixed latitude Antarctic plate (Fig. 1B) and a direct connection of the Pacific Plate and Campbell Plateau. The northward component of motion of the Campbell Plateau/Pacific Plate relative to Antarctica requires that the EPR move northward at the rate dictated by the spreading history of the Southwest Pacific Ridge, but does not account for either the longitudinal stability of the EPR or its history of asymmetric accretion.

Pacific Basin subduction buoyancy fluxes over the past 78 My

In a slab pull-dominated plate system, it is possible that the longitudinal stability of the EPR results from well-correlated (that is, effectively

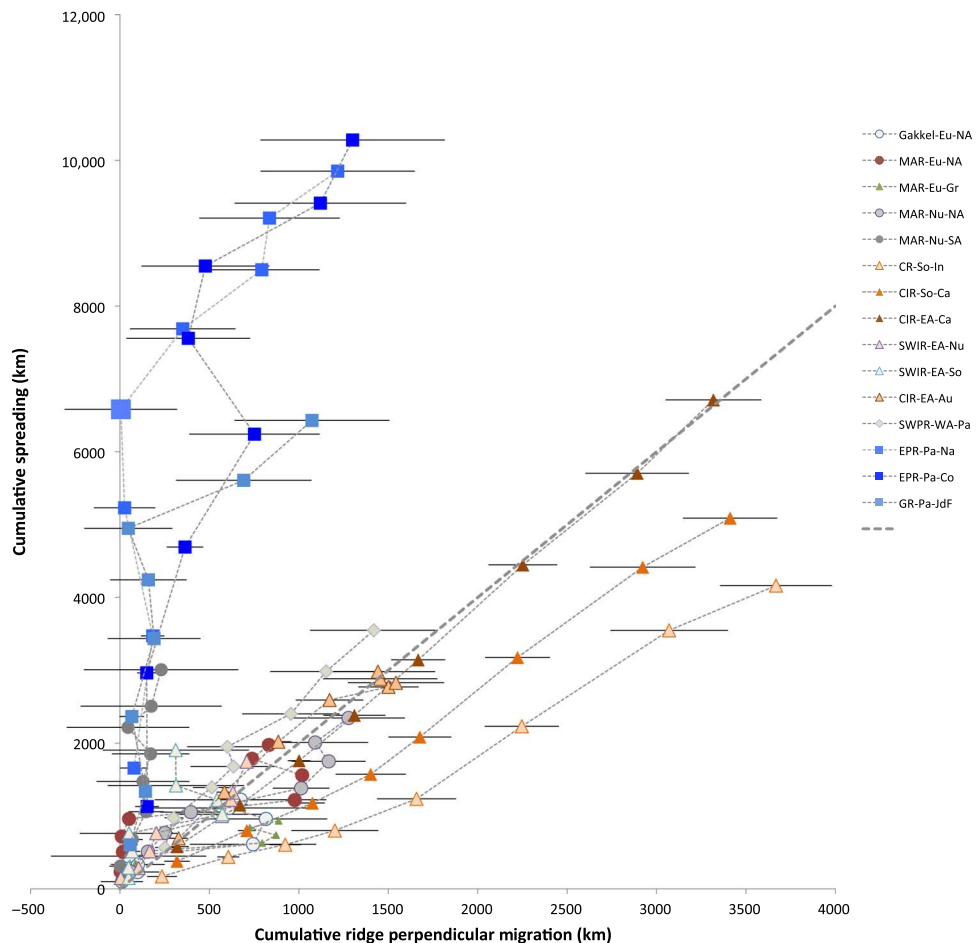


Fig. 4. Cumulative ridge-perpendicular migration relative to cumulative spreading at 10-Ma intervals from 10 Ma to 80 Ma. The thicker black dashed line (slope = 2) represents expected (half-spreading rate) ridge migration relative to a stationary plate. Horizontal error bars represent projections of the 95% confidence ellipses in the ridge-perpendicular direction. Ridges are MAR, Southwest Indian Ridge (SWIR), Central Indian Ridge (CIR), Carlsberg Ridge (CR), Southwest Pacific Ridge (SWPR), EPR, and Gorda Rise (GR). Plates are Eurasia (Eu), North America (NA), Greenland (Gr), Nubia (Nu), South America (SA), Somalia (So), India (In), Capricorn (Ca), East Antarctica (EA), Australia (Au), West Antarctica (WA), Pacific (Pa), Nazca/Farallon (Na), Cocos/Farallon (Co), and Juan de Fuca/Vancouver/Farallon (Jdf).

balanced or equal) subduction zone buoyancy fluxes of the plates on either side of the EPR as a function of time. The negative buoyancy of a subducting slab results from gravity operating on the density difference between the slab and adjacent mantle integrated over the volume of the slab (1). Assuming a simple tabular structure, the slab volume is the product of subduction zone length, down-dip length, and slab thickness. Slab thickness is small compared with subduction zone length. We assume that slab thickness is effectively constant and that small variations are unimportant. Forsyth and Uyeda argued that the “center of gravity” of the negative buoyancy force responsible for slab pull is at a depth of 200 to 300 km [(1), p. 169]. On the basis of their argument, the effective down-dip length is also small compared with subduction zone length. This leaves subduction zone length as the primary determinant of the slab volume. The proxy that we use also depends on the change in mean lithospheric density with square root of age (37). We have thus computed the mean of the square root of age of each subducting oceanic plate at the trenchward edge of each plate as a function of age of reconstruction. The buoyancy flux proxy thus depends on the effective length of the subduction zone times mean square root of age as a function of time. Effective length is the projected boundary length perpendicular to the relative veloc-

ity and is computed as the difference in great circle lengths projected from the instantaneous rotation axis to bounding triple junctions of each plate pair along each subduction zone segment as a function of age. As described by Turcotte and Schubert [(37); see section 6.22], this proxy is directly proportional to the slab pull force exerted on the descending lithosphere at ocean trenches.

In assessing the importance of slab buoyancy flux, we recognize that a number of resistive forces (for example, basal shear, collision resistance, and slab resistance) will operate to oppose the slab driving forces. The resistance forces must exactly balance the driving forces, and this balance determines the amplitude of the plate velocities generated by the driving forces. The plate velocities will thus be a linear function of the integrated driving forces acting on the plates. In the following, we parameterize the driving forces in terms of several proxies that represent the integrated slab pull acting on the Pacific and Farallon/Nazca plates, normalized by different measures of the resistance forces (see Materials and Methods for analytical details). Here, we simply summarize the results.

Comparing the proxies for subduction-related buoyancy flux of the Pacific and Farallon plates (Fig. 5) demonstrates that there is no simple relation between them. Also shown in Fig. 5 is the relationship

of these proxies when normalized by the respective areas of the plates as a function of age (see the Supplementary Materials). This normalization [previously adopted by Solomon *et al.* (38) in defining kinematic torques] is anticipated if the asthenosphere exerts a resistive drag force (basal shear) on the overlying plate and the amplitude of this drag force is proportional to the area of the plate. As shown in Fig. 5, independent of whether the subduction-related buoyancy is normalized by plate area, the Pacific and Farallon buoyancy fluxes are not balanced as shown by their departure from the 1:1 line. Both proxies in Fig. 5 show an overall trend with age that is from higher to lower values on the Pacific (*y*) axis in going from present to 78 Ma.

If, as typically assumed, the subduction rate of each plate correlates with the slab buoyancy flux of each plate, then (i) the spreading rate of the plates at the intervening ridge should correlate with the sum of the oppositely directed buoyancy fluxes (Fig. 5B). Furthermore, (ii) for a symmetrically spreading ridge, the ridge axes would be expected to move in the direction of the more negatively buoyant (hence, faster-moving) plate. Alternatively, (iii) asymmetric spreading could result in the ridge axis being fixed by accreting proportionately more to the faster-moving plate. Figure 5B shows that there is no relationship between the total buoyancy flux and spreading rate, and thus, expectation (i) is not satisfied. On the basis of this analysis, the fastest-spreading interval correlates with the lowest total buoyancy flux, opposite to expectation (i). The subduction-related buoyancy flux unscaled by plate area of the Pacific plate today is about five times greater than the Nazca, leading to the expectation that the EPR should be migrating rapidly westward [expectation (ii)] or should be characterized by large asymmetric spreading with faster accretion on the Pacific side [expectation (iii)]. Figure 5C shows the relationship between the Pacific slab buoyancy relative to Nazca (from 3 Ma to 20 Ma) and Farallon (from 21 Ma to 49 Ma) versus Pacific plate spreading fraction along the EPR. The ratio is always >1 in this interval, implying that the Pacific plate should be moving faster with faster spreading on the Pacific plate over this interval. However, the EPR is not migrating laterally over the past 40 Ma (Fig. 4), and the sense of asymmetry is opposite with Nazca/Farallon spreading exceeding Pacific by about 60 to 40% at least over the past ~50 My (Fig. 5C) (24). Normalizing the buoyancy flux ratio by plate area (Fig. 5C) is compatible with asymmetric spreading that favors the Nazca/Farallon plate, but the absence of correlation between the magnitude of spreading asymmetry and this ratio implies that this is not the primary controller. Figure 5C also shows that when this area-normalized buoyancy flux ratio is smallest, meaning Farallon slab pull should be greatest, then spreading is most symmetric. This is in contrast to expectation (iii). Thus, none of the expected correlations between subduction-related buoyancy fluxes and behavior of the EPR are supported by this analysis. This suggests that other mechanisms are controlling Pacific and Farallon plate motions, as well as the relative longitudinal fixity and dynamics of the EPR. We explore this using mantle flow calculations presented below.

Mantle flow calculations

The global mantle flow field presented below is calculated on the basis of joint seismic and geodynamic tomography inversions (39, 40) that map the spatial distribution of density in the mantle through a simultaneous inversion of seismic travel-time and global geodynamic data (40). These flow calculations incorporate combined convection-related and glacial isostatic constraints of the depth variation of mantle viscosity (41). An important aspect of these models is that plate motions

are not prescribed (that is, surface velocities are not imposed) but are predicted by integrating all the forces acting to drive the plates through their viscous coupling to the mantle-wide circulation (42). The fact that the modeled mantle flow is not forced by imposing the observed surface kinematics of the plates allows a direct test of the link between EPR behavior and mantle dynamics, which is the focus of the remainder of this section.

Inputs to global convective flow calculations:

Mantle viscosity

The basic procedure for predicting instantaneous (present-day) convective flow based on lateral heterogeneity provided by seismic tomography has been documented in numerous papers over the past three decades (43). The interested reader will find a detailed account of the fluid mechanical theory of tomography-based modeling of mantle dynamics that is used here to carry out the flow calculations presented by Forte (42). A comprehensive account of the theory used to carry out time-dependent simulations of mantle convection, using seismic tomography as a starting state, can be found in the study by Glišović *et al.* (44).

Tomography-based mantle convection modeling requires two fundamental inputs: (i) mantle viscosity and (ii) mantle density anomalies. In the following, we demonstrate the crucial importance of using input viscosity and buoyancy fields that are properly constrained to fit a wide suite of global geodynamic and seismic constraints. For this purpose, we explore the geodynamic consequences of using different inferences of mantle viscosity and mantle density anomalies used in recent studies of mantle dynamics.

We consider three mantle viscosity profiles that are shown in Fig. 6. Models V1 and V2 have both been determined by iterative, nonlinear inversions of global convection-related and glacial isostatic adjustment data (41). Model L4 is a four-layer parameterization of mantle viscosity originally derived by Behn *et al.* (45) in tomography-based mantle flow modeling of seismic anisotropy in oceanic regions. The L4 model, subsequently used by Conrad and Behn (46) and Conrad *et al.* (47), is characterized by a constant-viscosity lower mantle and a thick (200 km) asthenospheric viscosity channel with a viscosity that is 10 times lower than the upper mantle (300- to 670-km depth). A layer of strongly reduced viscosity in the asthenosphere also characterizes viscosity models V1 and L4. Model V1 is the only one that also has a low-viscosity layer at the bottom of the upper mantle. The asthenospheric viscosity reduction, expressed as a ratio of lithospheric to asthenospheric viscosity, is 300 for model L4, 80 for model V1, and 50 for model V2. Also, note that the lowest asthenospheric viscosity in model V2 is displaced to greater depth (300 km) relative to that in model V1 (at 150 km).

To illustrate the impact of these differing inferences of mantle viscosity, we calculate the mantle flow with a single model of three-dimensional (3D) density anomalies in the mantle, namely, model TX2008 derived by Simmons *et al.* (40), in a simultaneous inversion of global seismic and geodynamic data. This tomography model also includes constraints on thermal and compositional heterogeneity in the mantle provided by mineral physical data (see discussion below). In all cases, the surface plates are viscously coupled to the underlying mantle flow; therefore, their motions are not imposed but rather are predicted on the basis of the buoyancy-induced flow in the mantle. The geodynamic consistency of the predicted mantle flow may be quantified by determining the global variance reduction to the vector field of present-day plate velocities, described by NUVEL-1A in the

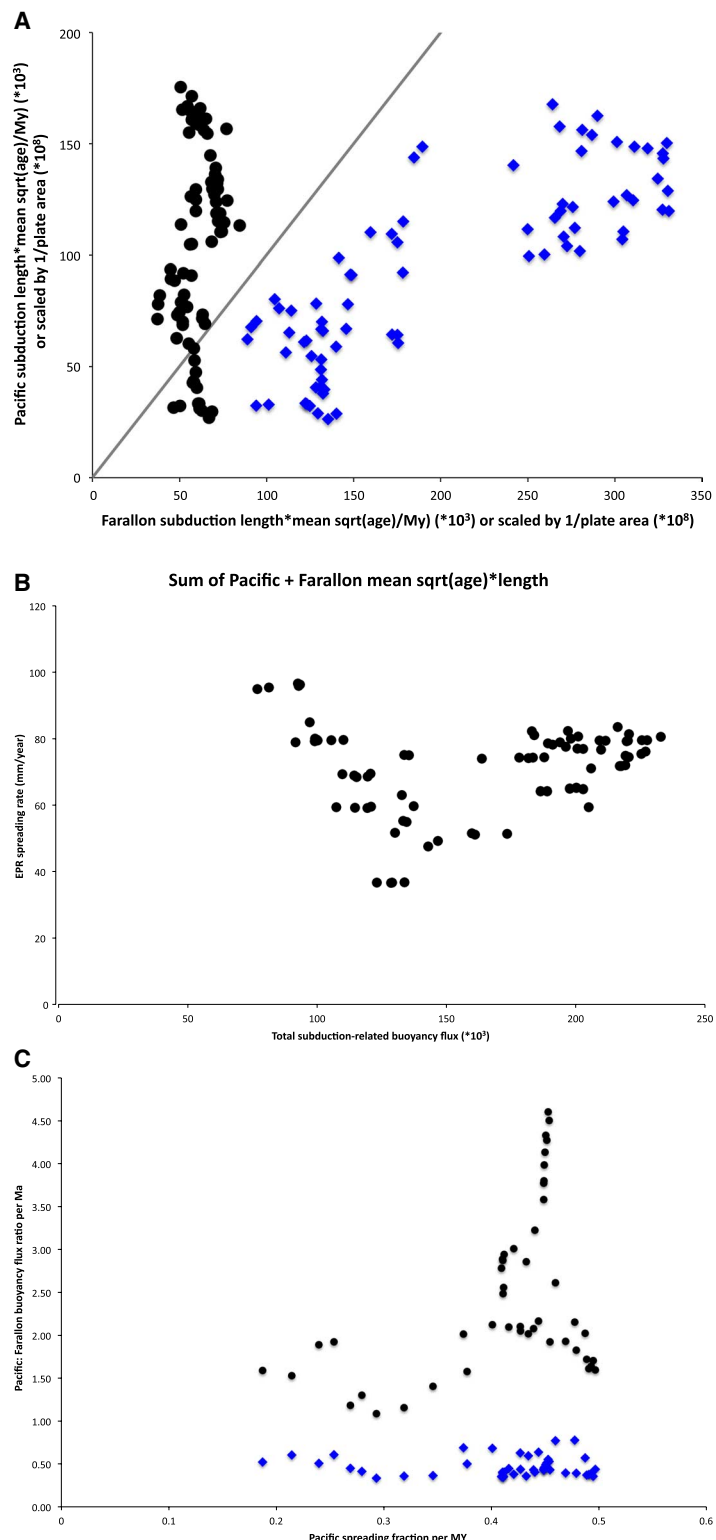


Fig. 5. Subduction-buoyancy flux in the Pacific basin. (A) Comparison of the subduction-related buoyancy flux proxy for the Pacific plate relative to the Farallon and Farallon-derived plates over the past 78 My. Each symbol represents the per My relationship. Black dots are not scaled by area, and blue diamonds are scaled by plate area as a function of age. Gray line is the 1:1 relationship. (B) Relationship of length-weighted mean spreading rate of the EPR as a function of age derived from plate boundary polygons (72) and associated rotations (73) and the sum of Pacific and Farallon plate subduction-related buoyancy flux as a function of age. Each dot represents the per My relationship in the interval from 0 to 78 Ma. (C) Pacific relative to Farallon plate subduction-related buoyancy flux ratio as a function of age versus Pacific Plate spreading rate fraction along the EPR as a function of age from 3 Ma to 49 Ma based on Rowan and Rowley (24) (black dots). Pacific relative to Farallon plate subduction-related buoyancy flux ratio normalized by plate area as a function of age (blue diamonds). Each symbol represents the per My relationship. Note that Pacific fraction is ≤ 0.5 , so Farallon is accreting asymmetrically faster.

NNR frame (48): 55% for viscosity model L4, 82% for model V2, and 90% for model V1. These variable matches between the predicted, mantle flow–driven plate motions and the observed plate motions suggest that there is an optimal range of viscosity reduction in the asthenosphere that yields a best fit. If this viscosity reduction is either too great or too low, then the fit to the plate motions will be degraded. The importance of a properly defined low-viscosity asthenosphere for generating and maintaining realistic, plate-like lithospheric motions has been recognized previously (49).

Although the predicted plate motions are an important convection-related observable that may be used to evaluate the geodynamic consistency or “realism” of the mantle flow models, there are other equally important observables, such as the dynamic surface topography, the free-air gravity anomalies, and the excess flattening or ellipticity of the CMB. We refer the interested reader to Forte (42) for a detailed discussion of these geodynamic observables and their use as constraints in convection modeling. In Table 1, we summarize the fits to this suite of geodynamic constraints for all three viscosity profiles, where, in each case, we use the same mantle density model TX2008 (40). Here, we note that the V1 profile results in an excellent and best overall fit to the combined set of geodynamic constraints, whereas the V2 profile provides a similar, though reduced, level of fit. Viscosity model L4 yields the least optimal fit.

The V2 profile, unlike V1, is characterized by a continuous variation of viscosity from the upper to the lower mantle. From the perspective of the predicted plate motions, the main difference between the V1 and V2 viscosities is that the latter has a thicker, higher viscosity lithosphere, which reduces the plate velocities (reflected in a reduced fit; see Table 1). From the perspective of deeper flow dynamics, the V2 profile has a higher viscosity in the bottom half of the lower mantle, yielding a more stable deep-mantle flow that has been extensively explored in the past numerical simulations of very long-term mantle convection (44, 50, 51). Unless otherwise specified, all mantle flow predictions discussed below use the V2 profile.

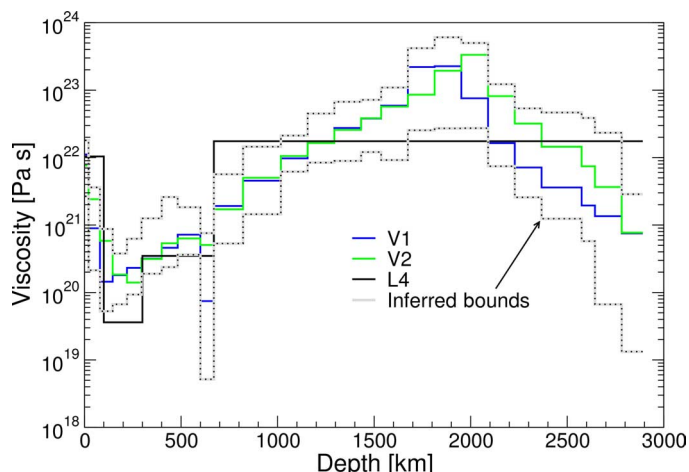


Fig. 6. Geodynamic inferences of mantle viscosity and implications for shallow mantle flow beneath the EPR. The solid blue and green curves, labeled V1 and V2, respectively, are the depth-dependent effective viscosities derived in Occam-style inversions of combined glacial isostatic adjustment and convection-related data sets (41). The dashed gray lines illustrate the 2σ uncertainties in the viscosity inference determined by varying the smoothing weights in the Occam inversions. The solid black curve, labeled L4, is a four-layer model (45) from fitting mantle flow to seismically inferred anisotropy below the African plate.

Inputs to global convective flow calculations: Mantle density anomalies

Although the previous discussion explored the effect of using different viscosity inferences, here we focus on the critically important issue of using a geodynamically consistent model of the 3D distribution of mantle density anomalies. To this end, we consider an independent model of long-wavelength mantle heterogeneity derived exclusively from the inversion of global seismic data, namely, model S20RTS (52), subsequently updated (53). This model has been extensively used in previous studies of tomography-based mantle flow, in particular the study of global mantle flow by Conrad *et al.* (47). In the following, we compare the S20RTS-based predictions of mantle flow with those based on the joint seismic-geodynamic tomography model TX2008 (40) discussed above.

The classical procedure for deriving 3D density anomalies from seismic tomography models is to rescale seismic velocity anomalies into equivalent density anomalies by using a simple multiplicative scaling factor that is typically assumed to be constant or depth-dependent in the mantle. A detailed discussion of this a posteriori density scaling of tomography models derived from seismic data alone is presented by Forte (42). For example, in the tomography-based flow models developed by Behn *et al.* (45), the seismic shear velocity anomalies in tomography model S20RTS are scaled to density using a constant (depth-independent) conversion coefficient of $0.15 \text{ (g/cm}^3\text{)}/(\text{km/s})$. These authors also assumed that density anomalies in the top 325 km of the mantle are zero. We have accordingly carried out a flow calculation using the same inputs for mantle density and the same parameterization of mantle viscosity, namely, model L4 (Fig. 6). The predicted flow reproduces essentially the same flow pattern as does that of Conrad *et al.* (47). We compare the convection-related observables discussed above, with predictions from these two models of the distribution of mantle density anomalies in Table 2.

These geodynamic observables place robust constraints on the integrated mantle buoyancy and viscosity structure. As shown by Forte *et al.* (54), the theoretical dependence of large-scale mantle flow on the integrated buoyancy distribution is similar to the dependence of the long-wavelength surface observables on the same buoyancy. In Table 2 (first and fourth rows), we thus quantify the fits to long-wavelength geodynamic data provided by the two mantle flow models.

Table 1. Global fits to convection-related observables, using TX2008 mantle density anomalies. All fits, with the exception of the CMB ellipticity, are expressed as percent variance reduction.

Viscosity model	Plate velocities*	Free-air gravity†	Geoid‡	Dynamic topography§	CMB ellipticity§
V1	90%	68%	99%	66%	430 m
V2	82%	61%	90%	65%	540 m
L4	55%	40%	41%	61%	690 m

*Fits between the predicted and NUVEL-1A vector field of plate velocities (48), in the NNR frame, are calculated on a global $5^\circ \times 5^\circ$ grid. †Fits are relative to the global free-air gravity and nonhydrostatic geoid anomalies derived from the GRACE geopotential solution (65), truncated at spherical harmonic degree 32.

‡Fits to the CRUST2.0-corrected dynamic topography (42) are for predicted and observed fields truncated at spherical harmonic degree 32. §The space-geodetic inference of excess CMB ellipticity is 400 m (76).

Although the flow model based on the constant density-velocity scaling of S20RTS provides a fair fit to the plate motions [equivalent to that obtained by a posteriori density scaling of other purely seismic tomography models (42)], it does not fit the other geodynamic constraints on mantle density structure. The fit to the long-wavelength geoid improves (see second row in Table 2) when the flow produced by S20RTS is modeled with a global free-slip surface boundary that is theoretically applicable only when tectonic plates are assumed to be absent [see detailed discussion by Forte (42)]. We note that Behn *et al.* (45) quote a global geoid variance reduction of 57% for the theoretical free-slip surface condition using an incompressible flow model. Our result in Table 2, for a compressible flow model, is slightly improved but comparable.

We can explicitly demonstrate that the misfit to the gravity data is mainly due to mantle density structure, and not the assumed viscosity, by calculating the geodynamic fits (see final row in Table 2) with the TX2008 joint tomography model and the L4 viscosity profile. The greatly improved fits to the geodynamic observables provided by TX2008 confirm the fundamental importance of the mantle density heterogeneity, particularly from the perspective of the gravity and equivalent geoid anomalies that provide crucial constraints on mid- and lower-mantle heterogeneity. It is the heterogeneity in this depth interval that provides the dominant contribution to the long-wavelength flow patterns. This exercise emphasizes the critical importance played by convection-related data in objectively establishing the reliability of a mantle flow model, in particular its relevance to the actual flow patterns in the mantle.

Deep-mantle buoyancy fluxes in relation to the EPR

On the basis of the above comparisons, mantle flow modeled with the TX2008 joint tomography model and the V1 and V2 viscosity profiles yield a good fit to the suite of geophysical observables discussed above. The relevance and utility of this tomography-based model of global mantle convective flow have been previously tested in regional studies that explored the links between the present-day and time-dependent flow (39, 55, 56) over the past 30 My. This global flow model has also been tested in direct comparisons of time-dependent topography predictions with detailed geological constraints on the variable uplift of the U.S. Atlantic Coastal Plain since the mid-Pliocene (57). Finally, this flow model has also served as a starting point for very long time simulations of thermal convection, which reveal the longevity and geographic fixity of a number of mantle-wide thermal upwellings that correlate with surface hot spot locations and are maintained over hundreds of millions of years by high CMB heat flux (44, 50). On the basis of these multiple comparisons of model predictions and observation of the global mantle flow, we now return our focus to the specific predictions related to the EPR.

Much emphasis has been placed on the large regions with seismically slow velocities in the deep mantle beneath the central Pacific and Africa [sometimes referred to as large low-shear velocity provinces (LLSVPs)] (Fig. 7); however, the region of slow velocities beneath the eastern Pacific has gained substantially less attention. Figure 7 shows that the estimated radial flow velocity at 2685-km depth in the mantle, at the top of the seismic D'' layer, is higher beneath the EPR than beneath South Africa, West Africa (39), and the central Pacific, despite the fact that the amplitude of the V_s anomaly in this region is not larger than the amplitudes associated with the Pacific and Africa LLSVPs. This reflects the much smaller compositional (intrinsically dense) contribution to the mantle heterogeneity below the EPR relative to the other low-shear velocity zones (58).

Maps of upper-mantle (Fig. 7, A and B) and lower-mantle flow (Fig. 7C) show that the EPR is the only mid-ocean ridge boundary that is spatially correlated with strong upwelling at all depths. For example, at 650-km depth (Figs. 1 and 7B), the EPR is underlain by the strongest region of upwelling at this depth in the mantle, with secondary foci near the Nazca-Cocos-Pacific triple junction and the Chile Rise. We note that the other ridge with the long RRTs, the southern MAR, is also correlated with relatively strong radial flow at depth. We thus find that the EPR and MAR, which overlie active upwellings, contrast with other ridges that are responding passively to plate divergence and are instead controlled by a combination of mantle drag and slab pull.

A cross section through the predicted present-day mantle flow field (Fig. 8B) shows that the upper- and lower-mantle flow in Fig. 7 are connected beneath the EPR by continuous radial flow with velocities in excess of 50 km/My from the CMB to the surface. These flow calculations thus suggest very strong upwelling beneath the EPR that is compatible with seismically inferred V_s anisotropy beneath the EPR at depths of 200 to 300 km (59, 60). The dominant control of the internal buoyancy distribution in driving this mantle-wide upwelling under the EPR can be demonstrated by calculating the mantle flow in the presence of a global rigid-surface boundary condition, as shown in Fig. 8C. The peak amplitude of the upwelling remains directly under the surface location of the EPR, although the latter is no longer modeled as a plate boundary (that is, weak zone) in this test simulation. The plate-coupled and rigid-surface calculations (Fig. 8, B and C) show very similar patterns and amplitudes of flow in the deep

Table 2. Global fits to long-wavelength ($\ell = 20$) convection-related observables. All fits, with the exception of the CMB ellipticity, are expressed as percent variance reduction, where the predicted and observed fields are truncated at spherical harmonic degree $\ell = 20$. N/A, not applicable.

Flow model	Plate velocities*	Free-air gravity	Geoid	Dynamic topography	CMB ellipticity**
S20RTS + L4 [†]	44%	-7%	-60%	-50%	1440 m
S20RTS _{r-s} + L4 [‡]	N/A	12%	64%	-17%	1430 m
S20RTS _{inv} + V2 [§]	48%	28%	57%	40%	450 m
TX2008 + V2 [¶]	80%	74%	90%	73%	540 m
TX2008 + L4	60%	50%	41%	69%	690 m

*Fits between the predicted and NUVEL-1A vector field of plate velocities (48) in the NNR frame are calculated on a global $5^\circ \times 5^\circ$ grid. †Fits are calculated for the flow model using a posteriori density conversion of tomography model S20RTS used by Behn *et al.* (45) and L4 viscosity model (Fig. 6). Plate motions are viscously coupled to underlying mantle flow.

‡Fits are calculated for a theoretical free-slip surface boundary condition (no surface plates) using identical density and viscosity inputs as in the previous footnote (see previous model above). §Fits are calculated for the flow model using optimized density-velocity scaling of model S20RTS from Occam inversion of surface geodynamic data (42) and using V2 viscosity model (Fig. 5). Plate motions are viscously coupled to underlying mantle flow.

¶Fits are calculated for the flow model using the TX2008 density heterogeneity model and the V2 viscosity model. Plate motions are viscously coupled to underlying mantle flow.

||Fits are calculated for the flow model using the TX2008 density heterogeneity model and the L4 viscosity model. Plate motions are viscously coupled to underlying mantle flow.

**The space-geodetic inference of excess CMB ellipticity is 400 m (76).

mantle, thereby ruling out the control of the surface plates on the deep EPR upwelling shown in Fig. 8B.

The outstanding question is whether the strong upwelling under the present-day EPR revealed by the instantaneous flow calculations (Figs. 7 and 8B) is sufficiently long-lived and stable to account for the lateral fixity of the EPR on the same time scale (~80 My) revealed by the plate kinematic analysis in Figs. 1, 3, and 4. Time-reversed convection simulations initiated with the same model of present-day flow used here (55, 57, 61) show that the location of the peak amplitude mantle upwelling under the EPR has been stable for at least the past 30 My. The recent time-reversed convection models by Glisovic and Forte (51) show that mantle-wide flow centered directly below the EPR axis has been active for at least the past 65 My. In Fig. 8A, the radial flow below the EPR at -55 Ma extends from the CMB directly to the surface with no lateral displacement relative to the axis of present-day upwelling.

The behavior of the mantle below the EPR over longer time spans can be explored by forward integrating the present-day mantle density distribution and associated flow, as in recent, very long-time thermal convection simulations (44). Figure 8D shows the evolution of the EPR upwelling after a 100-My integration, in which a simple rigid-surface boundary is again used to rule out any potential bias from assumed plate-boundary locations. To simulate the broader, smoother structure derived from seismic tomography (Fig. 8, B and C) due to the smoothing and damping inherent in the global tomography inversions (62), we passed the theoretical flow prediction in Fig. 8D through a “tomographic filter” (62). We again note that the location of the upwelling is closely correlated with the present-day EPR location, thus demonstrating the long-lived internal buoyancy in this region of the mantle. This stability or “anchoring” of the EPR upwelling is a fundamental consequence of the high-viscosity lower mantle that characterizes the geodynamically inferred viscosity profile used in the convection model (see Fig. 6).

Asymmetric spreading is another aspect of EPR kinematics that can be understood in terms of the asthenospheric flow patterns predicted by our global mantle convection model. Again, we emphasize that the plate motions are predicted by the model and not prescribed. Figure 9 provides a close-up view of the horizontal and radial flow at 250-km depth, in the same cross section where the asymmetry in flow away from the EPR is strongly pronounced (Fig. 8B). This figure shows that the horizontal component in sub-Nazca asthenosphere flows more rapidly eastward than sub-Pacific asthenosphere flows westward (at equal distances from the EPR axis). The fundamental contribution to this asymmetry from the integrated buoyancy in the mantle is made evident by the flow calculation in Fig. 9C, where a rigid-surface boundary condition is assumed; hence, there is no feedback from a weak surface plate boundary. Figure 9D shows the persistence in the model of this asymmetric divergence after a 100-Ma forward integration with a rigid boundary layer, as shown in Fig. 8D.

The horizontal flow predicted under the EPR along the same mantle cross section shown in Figs. 8 and 9 is demonstrated in Fig. 10A for the three different mantle viscosity profiles to assess the role of viscosity in these results. The flow is plotted at two depths, 50 and 250 km, corresponding to the mid-lithosphere and asthenosphere, respectively. We note that all three viscosity profiles yield a strong asymmetry in the horizontal component of asthenospheric flow relative to the surface location of the EPR. This asymmetry emerges because the reduction of viscosity in the asthenosphere is sufficiently large to allow the deeper buoyancy-driven flow to strongly influence the flow pattern in the asthenosphere. Hence, the source of the

asymmetry is from the mantle buoyancy distribution and not from the plate-boundary condition at the surface (compare Fig. 9, B and C).

Our model of mantle flow viscously couples the plates to the underlying mantle flow. This allows for the direct comparison of the relative velocities of the asthenosphere and overlying lithosphere. As shown in Fig. 10A, for viscosity profiles with a sufficiently large

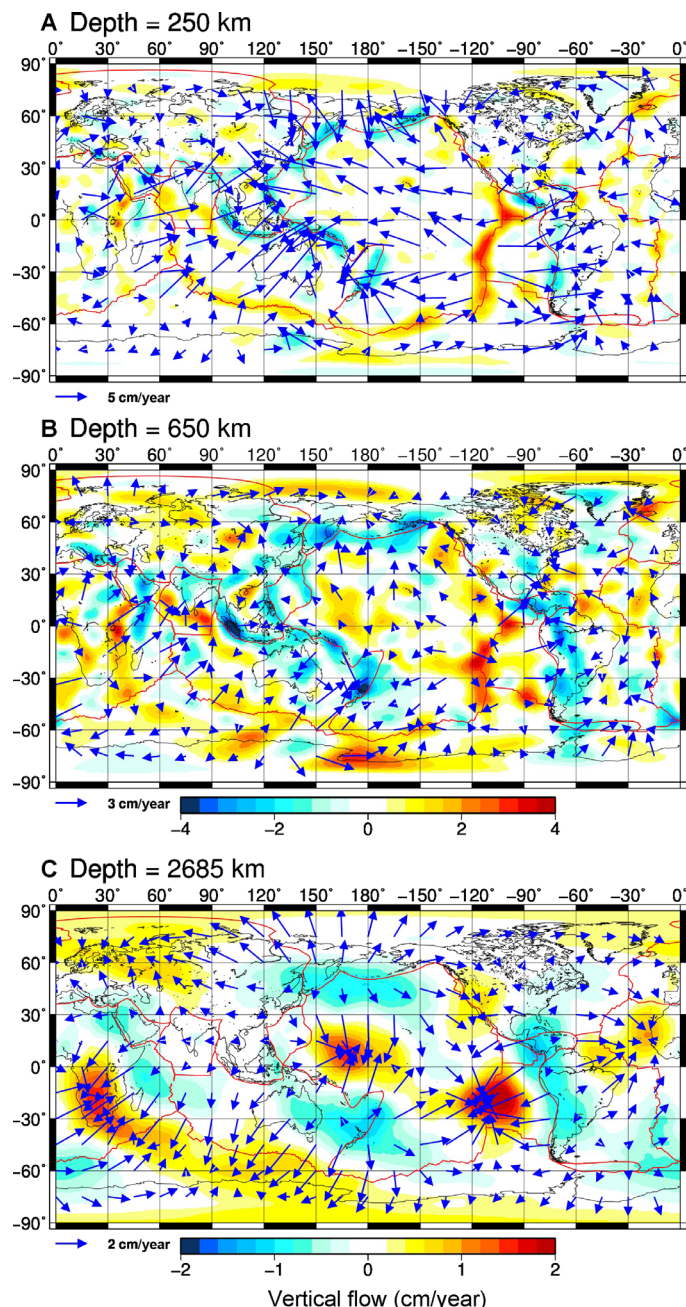


Fig. 7. Predicted present-day convective flow at three different depths in the mantle. (A) Asthenosphere. (B) Base of the transition zone. (C) Top of the seismic D'' layer. The mantle buoyancy distribution is given by model TX2008, obtained from joint seismic-geodynamic inversions by Simmons *et al.* (40). The viscous response of the mantle is calculated on the basis of the “V2” viscosity profile (39), derived from the joint glacial isostatic adjustment convection inversions (41) shown in Fig. 6. The flow calculations are described in detail by Forte *et al.* (39).

Coupled surface plates

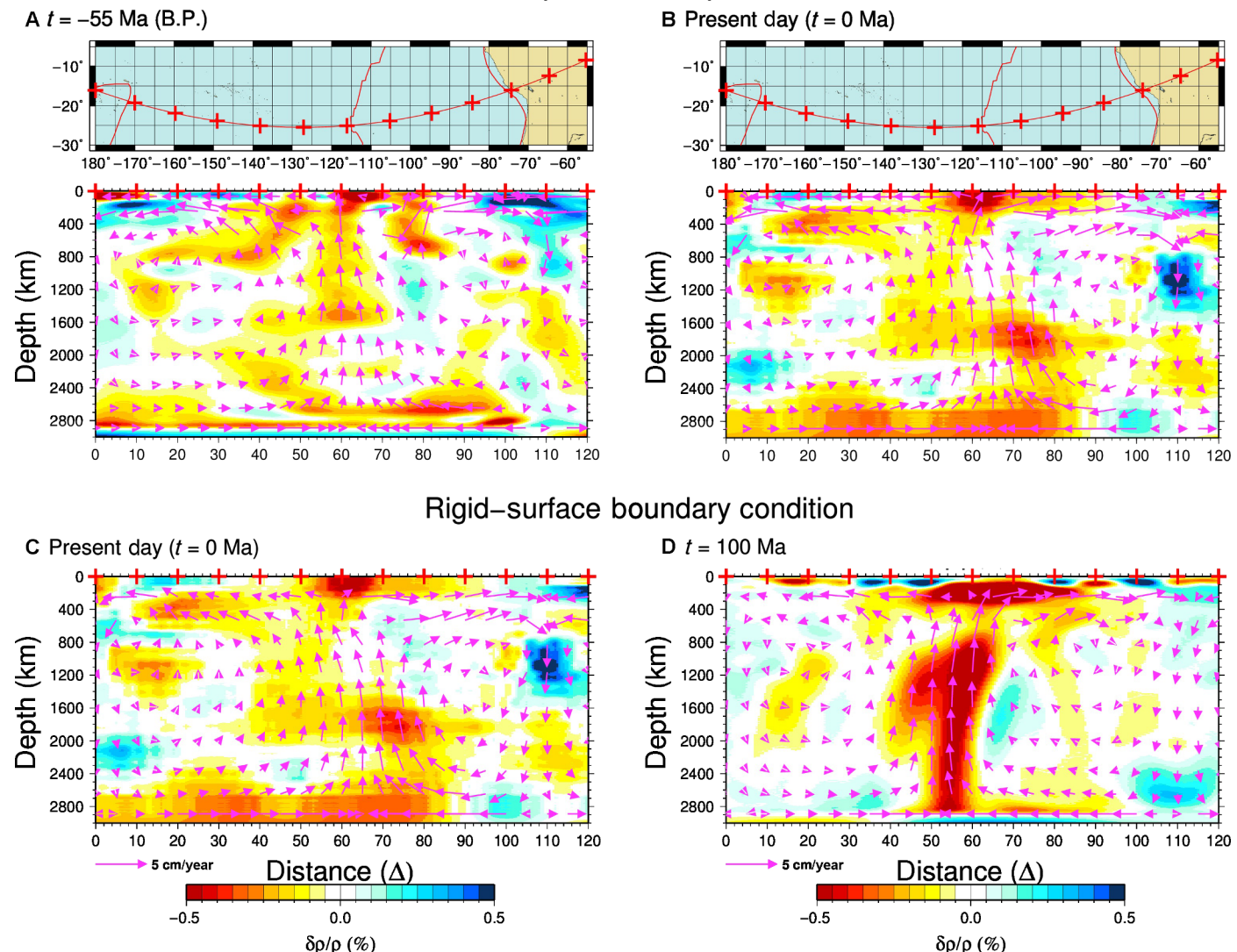


Fig. 8. Cross sections across the EPR showing mantle density anomalies as a function of depth together with computed flow velocities. (A) Mantle flow at -55 Ma [before the present (B.P.)] predicted on the basis of a tomography-based, time-reversed mantle convection simulation (51) that is initiated with the same present-day flow shown in Fig. 7, based on the joint tomography model TX2008 (40) and geodynamically inferred V2 viscosity profile (Fig. 6). (B) Present-day mantle flow with surface plates whose motions are predicted on the basis of viscous coupling to the underlying buoyancy-driven flow in the mantle. This is the same flow calculation used in Fig. 7 that also serves as the starting point for the time-reversed simulation in (A). (C) Present-day mantle flow calculated with a global, rigid-surface boundary condition. All other inputs (for example, mantle buoyancy and viscosity structure) are identical to those used in (B). (D) Evolution of the flow pattern shown in (C) after 100 My, calculated by forward integration in the tomography-based mantle convection simulations with a rigid-surface boundary condition by Glišović *et al.* (44) and subsequently filtered to maximum harmonic degree 32 to simulate the effective filtering arising from the tomographic inverse procedure (62). The amplitude spectrum of this filtered prediction agrees closely with the present-day structure in (B).

reduction in sublithospheric viscosity, the computed horizontal flow velocity in the asthenosphere exceeds that of the overlying lithosphere. This is also seen in our models of flow globally [for example, Forte (8) and Forte *et al.* (39)]. Thus, rather than the asthenosphere that is entrained passively by the motion of the overlying plates, horizontal tractions due to more rapid asthenospheric motions driven by deep-mantle buoyancy are actually a significant contributor to plate motions (8, 63). Our flow modeling suggests that the asymmetric lithospheric movement at the EPR is controlled by differential flow velocities within the asthenosphere and not by far-field forces transmitted through the lithosphere. The impor-

tance of deep buoyancy in driving the observed plate motions is explored in Fig. 10B, where we find, for the V1 flow calculations, that eliminating positive buoyancy below the EPR in the lower mantle leads to a $\sim 40\%$ reduction of horizontal motion for the Nazca plate and a $\sim 25\%$ reduction for the Pacific plate. If all positive buoyancy below 250-km depth is eliminated, then Nazca and Pacific motions are reduced by ~ 70 and $\sim 40\%$, respectively. These tests further illustrate the important degree to which deep-mantle buoyancy beneath the EPR is controlling the present and longer-term evolution of the EPR and contributing to plate driving forces, a major conclusion of this paper.

Coupled surface plates

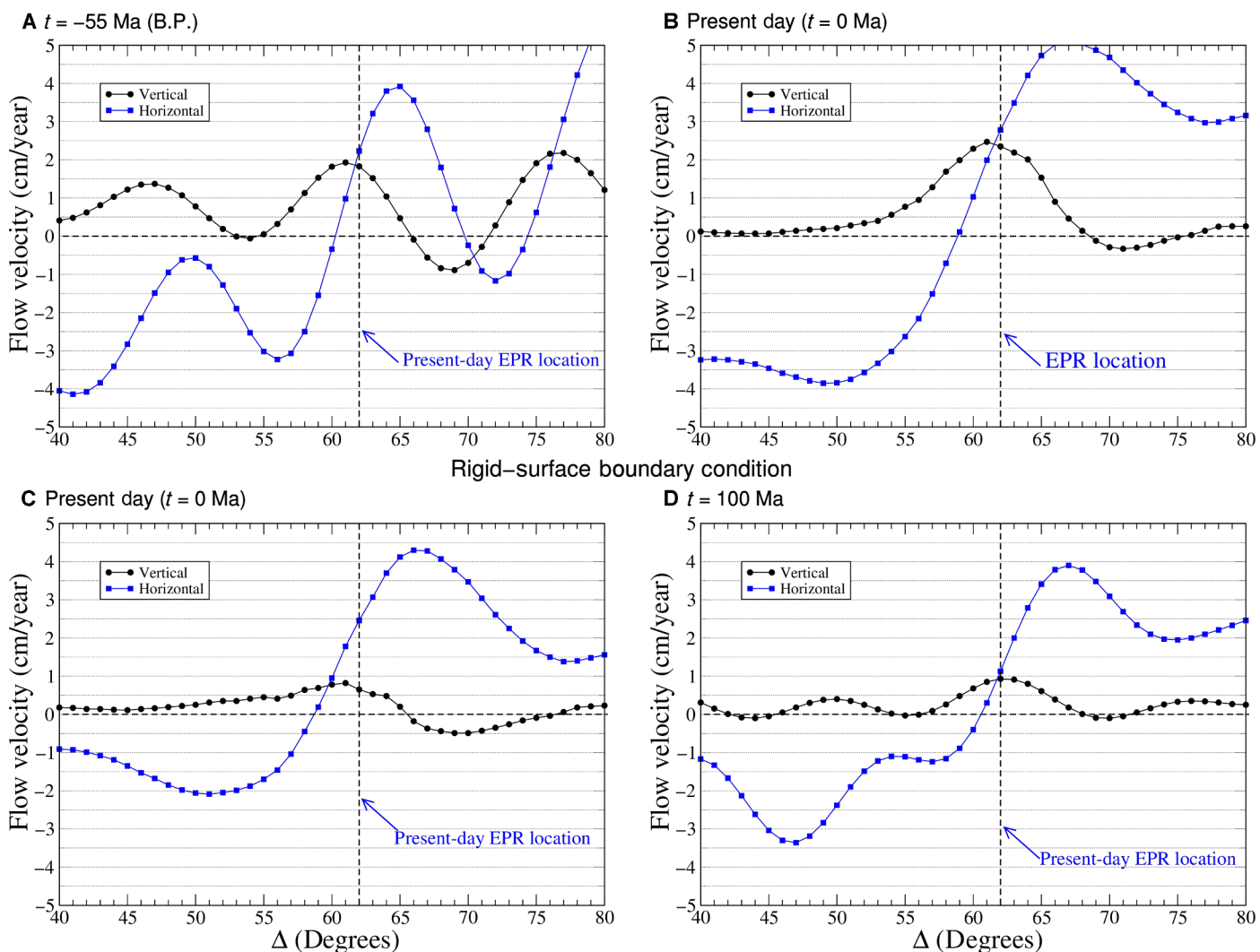


Fig. 9. Cross sections across the EPR showing the vertical and horizontal components of buoyancy-driven asthenospheric flow at 250-km depth. The blue curves in (A) to (D) show the component of the horizontal flow in the plane of the cross sections presented in Fig. 8. The black curves show the vertical component of the flow.

DISCUSSION

We synthesize the dynamical arguments by integrating the map and cross-sectional representations of Figs. 7 and 9 into a 3D perspective of the buoyancy distribution and corresponding present-day mantle flow field within the eastern Pacific realm (Fig. 11). This shows the complex and spatially varying distribution of buoyancy throughout the mantle. Despite this spatial variability, the resulting flow field is relatively simple. The pattern of flow under the Nazca plate is represented by a classical convective roll aligned with the axis of the EPR. The convective structure under the Pacific is more diffuse, reflecting in part the greater lateral distances to the bounding subduction zones to the west (see Fig. 8B). The strong radial velocities associated with this convective roll asymmetrically diverge in the asthenosphere and viscously couple to the overlying plates to contribute to their relative motions. Figure 11 also emphasizes the strong spatial correlation of the deep-mantle buoyant material with the location of the EPR. The resulting mantle flow field thus provides the dynamical explanation for the kinematic observation of the relative longitudinal fixity and asymmetric spreading of the EPR.

The model of mantle flow in Fig. 11 differs markedly from other analyses of the mantle flow in this part of the eastern Pacific (47). We reproduce in Fig. 12 the results of previous work by Conrad *et al.* (47), based on our reproduction of their calculations. In this other analysis of Pacific mantle flow, Conrad *et al.* (47) argue that the EPR is spatially disconnected by some 30° from the larger-scale mantle upwelling that is centered in their calculations on the Southwest Pacific Superswell (Fig. 12A) and therefore that EPR spreading is independent of the large-scale mantle flow, contrary to the conclusions presented above. To objectively compare their predictions with ours, we present below a suite of further tests of their predictions relative to ours and, in turn, relative to observations.

The origin of the 30° shift is clear when the density anomaly distributions are compared in the cross sections (Fig. 12, A and B). The a posteriori conversion of tomography model S20RTS into an equivalent density model using a constant value for the density-velocity scaling results in a buoyancy distribution with maximum amplitudes displaced westward of the buoyancy distribution given by model TX2008,

obtained from the joint seismic-geodynamic tomography inversions. The crucial role of the mantle density anomalies in determining the basic pattern of mantle flow, independent of the details in the radial viscosity profile, is demonstrated in Fig. 12D, where we show the flow field predicted on the basis of the TX2008 model of mantle density heterogeneity and the L4 viscosity profile. Comparison of

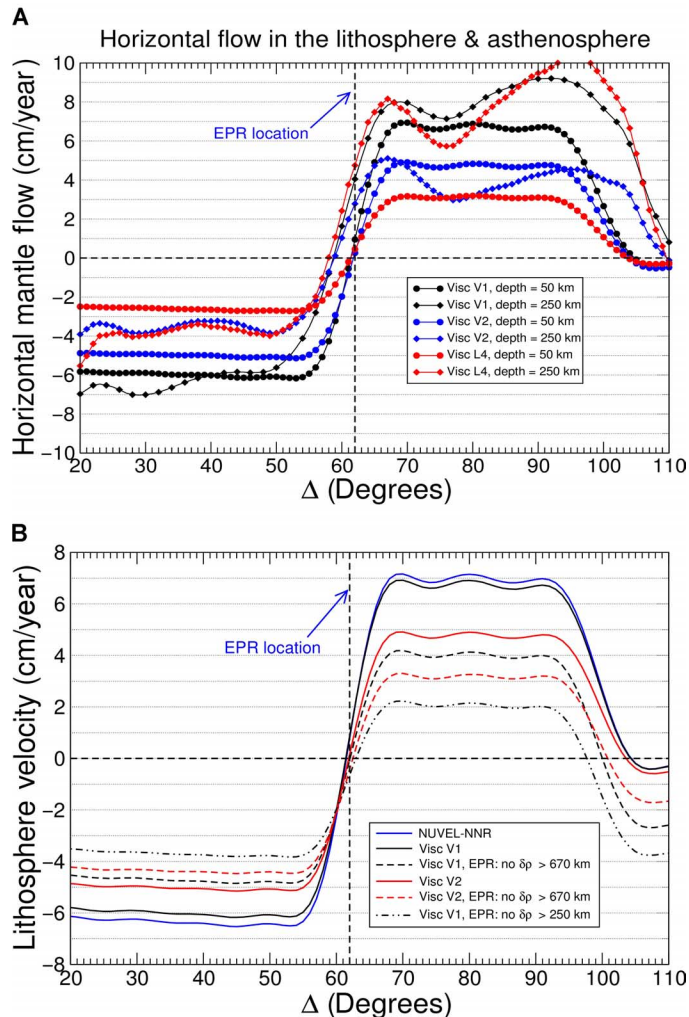


Fig. 10. Horizontal components of lithosphere and asthenosphere flow. (A) Horizontal component of mantle flow under the EPR region in the mid-lithosphere (50-km depth) and asthenosphere (250-km depth) calculated using the three viscosity profiles in Fig. 6. In each case, the mantle density anomalies are from the joint seismic-geodynamic tomography model TX2008 (40). The flow is represented in the same mantle cross section as in Figs. 8 and 9. Positive and negative values indicate eastward- and westward-directed flow, respectively. (B) Observed and predicted surface lithospheric flow velocity, projected onto the same cross section, as in (A). The blue curve represents the NUVEL-1A plate velocity in the NNR reference frame. The black and red curves show the prediction obtained using the V1 and V2 viscosity profiles, respectively (Fig. 6). The dashed curves show the predicted lithospheric velocity when we remove the positive buoyancy below the EPR at all depths in the lower mantle (curves labeled $\delta\rho > 670$ km) and at all depths below the asthenosphere (curve labeled $\delta\rho > 250$ km). In these flow tests, we searched and removed all positive buoyancy in a geographic region centered on the EPR axis, extending from 20°N to 50°S and from 90°W to 120°W. In all cases, the lithospheric flow is represented up to spherical harmonic degree 32 (hence, the slight oscillations in the flow profiles).

Fig. 12 (B and D) reveals a strong similarity in the calculated flows, despite the different viscosity profiles used in each case.

We can attempt to optimize the match to the suite of surface geodynamic data (listed in Table 2) provided by purely seismic tomography model S20RTS by inferring the optimal depth-dependent density-velocity scaling, via an Occam inversion [details of such an inversion are presented by Forte (42)]. The resulting buoyancy distribution and associated flow field are shown in Fig. 12C, and the geodynamic fits are summarized in Table 2 (third row). We note that the flow field is again characterized by a peak upwelling located westward of that predicted using the TX2008 model (see Fig. 12, B and D). However, note that much of the buoyancy in the lower mantle has been strongly reduced, because the geodynamic data—especially the long-wavelength gravity anomalies—place strong constraints on the total buoyancy at these depths and hence can resolve the presence of compositional contributions to total density. As is evident in Fig. 12C, the compositional contributions are inferred to reduce total density in the deep mantle under the central Pacific. However, the fundamental problem is that a constant density-velocity scaling, or even one that varies with depth, is simply not sufficient to resolve the laterally variable effect of compositional heterogeneity that lies at the center of the large-scale, lower-mantle anomaly under the south central Pacific (40, 58). The origin of this compositional heterogeneity has been interpreted in terms of an evolving “chemical pile” under the central Pacific [for example, McNamara and Zhong (64)].

The detailed analysis of Simmons *et al.* (58) demonstrates that a successful reconciliation of the constraints on 3D mantle structure by seismic data with the independent constraints provided by geodynamic data requires the inclusion of significant lateral variations in density-velocity scaling. These lateral variations model the effects of nonthermal or compositional heterogeneity in the lower mantle, in addition to thermally generated density anomalies. This compositional buoyancy is important in opposing or cancelling the excess buoyancy that would otherwise be generated on the assumption of pure thermal buoyancy. The latter assumption is implicit in the use of a constant lower-mantle density-velocity scaling by Conrad *et al.* (47). Properly accounting for the geographically localized impact of lower-mantle chemical heterogeneity requires the use of a laterally variable density-velocity scaling, as in model TX2008. The explicit signature of this nonthermal, intrinsically dense, lower-mantle heterogeneity under

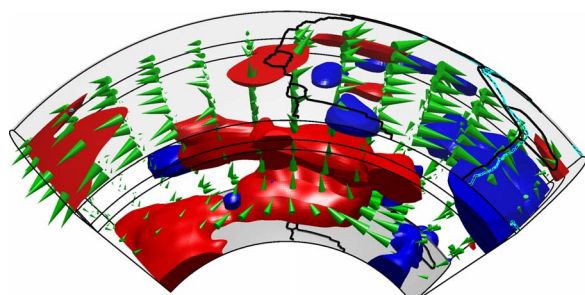


Fig. 11. 3D representation of the buoyancy distribution (shaded volumes) and corresponding flow field (cones) centered on the EPR. Lower boundary is the CMB, and upper boundary is the surface of Earth. Black lines are plate boundaries from Bird (75). Coastline of South America is shown as the speckled line. Blue shaded volumes are characterized by $\delta\rho/\rho \geq 0.1$, and red shaded volumes are $\delta\rho/\rho \leq -0.1$. Axes of the cones point in flow direction, and the size is proportional to the velocity. Note the clear asymmetry of the flow velocities on either side of the EPR.

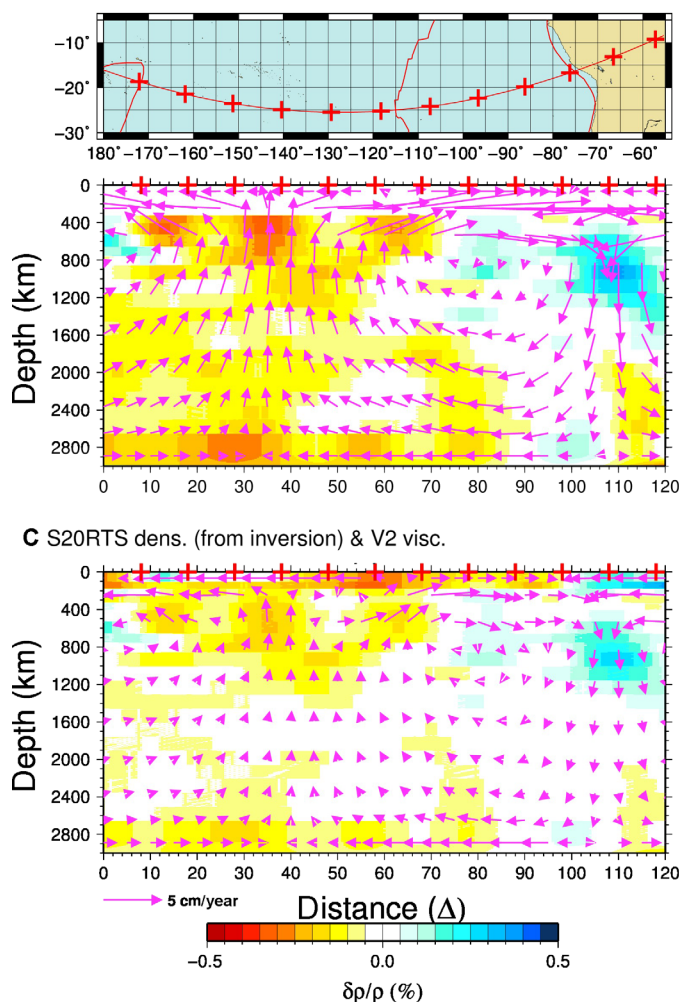
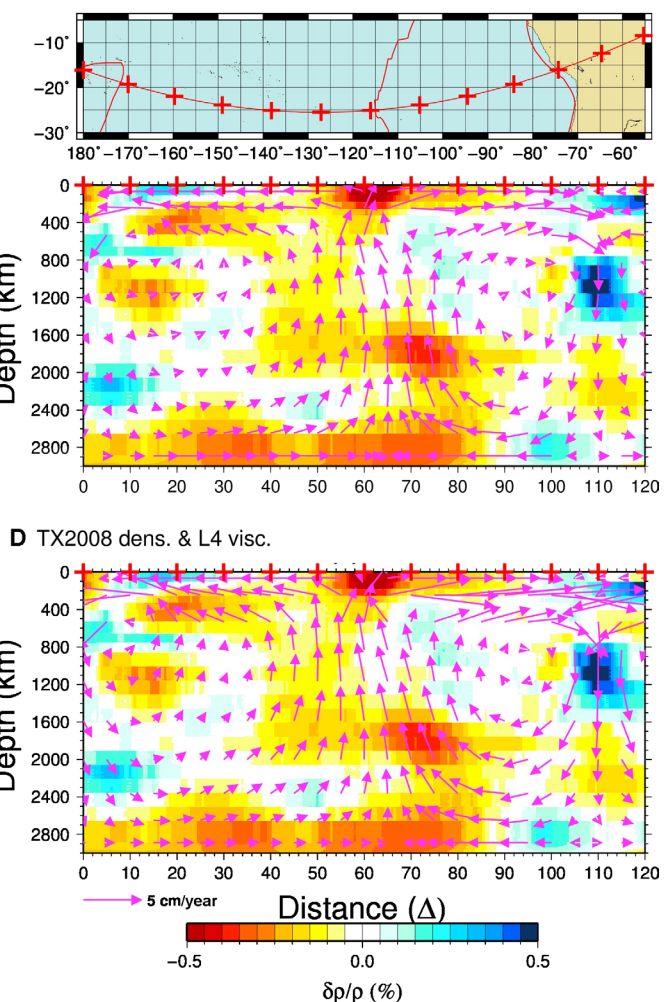
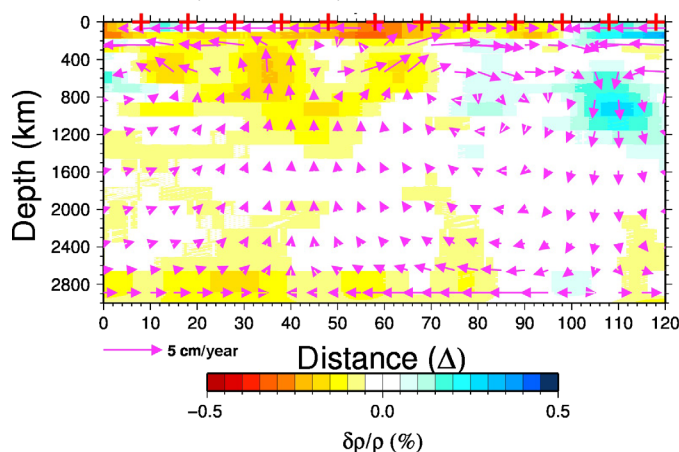
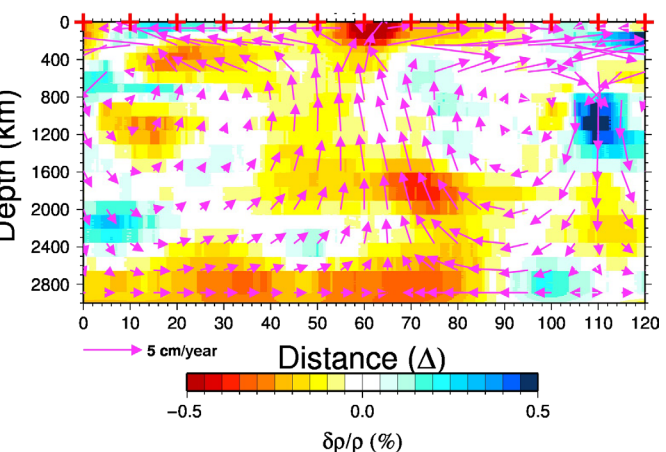
A S20RTS dens. & L4 visc.**B** TX2008 dens. & V2 visc.**C** S20RTS dens. (from inversion) & V2 visc.**D** TX2008 dens. & L4 visc.

Fig. 12. Dependence of mantle flow under EPR on distribution of deep-mantle buoyancy. (A) Mantle flow predicted on the basis of the S20RTS tomography model converted to density using the constant density-velocity scaling used by Behn *et al.* (45) and Conrad and Behn (46). The L4 viscosity profile (see Fig. 6) is used in this calculation. (B) Mantle flow predicted using the density anomalies from the TX2008 tomography model (40) and the V2 viscosity profile (see Fig. 7). (C) Mantle flow predicted using an optimized, Occam-inverted, depth-dependent density-velocity scaling [see Forte (42) for details] of the S20RTS tomography model. The V2 viscosity profile is used in this calculation. (D) Mantle flow predicted using the TX2008 density anomalies and the L4 viscosity profile. The mantle cross section used here is identical to that in Fig. 8.

the Pacific plate is underlined by the most recent joint seismic-geodynamic inversions by Simmons *et al.* (58).

Free-air gravity anomalies provide a robust constraint on internal density anomalies. Here, we illustrate how these gravity anomalies can be used to discriminate between the buoyancy distribution derived from the density-velocity scaling of S20RTS, used by Conrad *et al.* (47), and model TX2008 derived via the joint seismic-geodynamic inversion procedure developed by Simmons *et al.* (58). This is an important issue because the mantle density anomalies that generate the gravity anomalies are also the very same anomalies that drive the mantle flow and plate motions. To have confidence that the latter is properly modeled, the gravity constraints must be satisfied.

The free-air gravity anomalies predicted on the basis of Conrad *et al.*'s (47) flow model (Fig. 12A) and the flow model obtained on the basis of the TX2008 density anomalies (Fig. 12B) are presented in Fig. 13. Figure 13A shows the observed free-air gravity anomalies in the central and eastern Pacific derived from Gravity Recovery and Climate

Experiment (GRACE) data (65). The free-air gravity anomalies predicted with the TX2008-based flow model in Fig. 12B are shown in Fig. 13B; they provide a 75% variance reduction to the Pacific region GRACE data (better than the global-scale fit summarized in Table 1). The gravity anomalies predicted with the S20RTS-based flow model in Fig. 13A are shown in Fig. 13C; they provide a ~80% variance reduction (that is, a variance increase) to the data. In Fig. 13D, we also explore a prediction using a simple free-slip surface boundary—hence, no plate motions can be explained—and we find that the variance reduction is 20% (compared to the global-scale fit of 12% in Table 2). This is obviously an improvement relative to the complete misfit provided by the prediction in Fig. 12C but is inferior to the fit obtained with TX2008-based flow model.

On the basis of this analysis of Pacific region GRACE free-air gravity anomalies, the mantle flow predicted with the TX2008 tomography model provides a geodynamically consistent mantle flow prediction in which the main focus of mantle upwelling in the eastern

Pacific is directly under the EPR and not under the south central Pacific. The inference derived by Conrad *et al.* (47) that the flow under the EPR is subhorizontal from west to east, from above the Pacific Superswell toward, across, and under the EPR, is therefore contradicted by the analysis presented here.

The longevity and stability of this upwelling (Fig. 8), reflected in the kinematic behavior of the EPR (Fig. 1), are the most important finding of the work presented in this study. Our flow modeling suggests that a long-lived buoyancy distribution under the EPR is responsible for the lateral stability of the main southern segment of the EPR system and that it generates asymmetric plate separation. The asymmetry in predicted asthenospheric flow under the EPR (Fig. 8) is most strongly expressed when there is a sufficiently large reduction in the viscosity of the asthenosphere relative to the lithosphere (Fig. 10A). Viscous coupling of the overlying plates to the underlying asthenospheric flow results in a corresponding asymmetry in plate diver-

gence along the EPR (Fig. 10B). We emphasize that this asymmetry in predicted plate motions is not imposed but simply arises from the integrated positive buoyancy under the EPR that also generates the mantle-wide upwelling.

We regard the phenomenon of plate accretion at the EPR as being physically distinct from the phenomenon of mantle or lithospheric flow. The latter is simply a product of the integrated buoyancy forces in the mantle, whereas the former is a complex thermomechanical process that depends on partial melting and magma transport, as shown in modeling by Mittelstaedt *et al.* (66). These authors show how the accretion process may allow a ridge to be “pinned” to a stationary mantle upwelling through asymmetric spreading and plate creation. They find that magmatic heating, plate age, and spreading rate are factors that influence ridge-plume interactions. In particular, they find that the process of ridge jumping is enhanced by increases in the volume flux of the plume, resulting in greater melt flux and greater

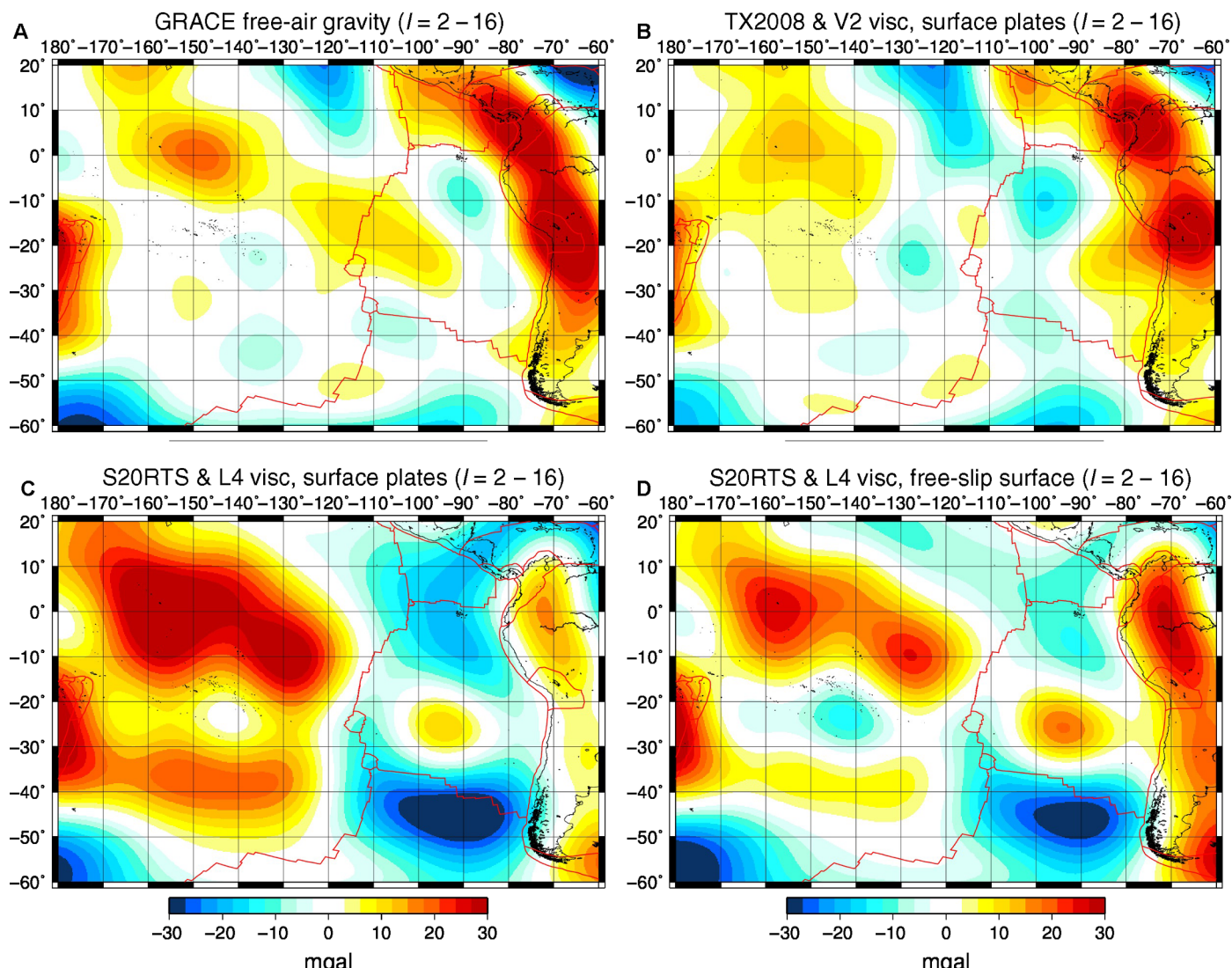


Fig. 13. Free-air gravity anomalies in the central and eastern Pacific. (A) Observed free-air gravity anomalies from the GRACE geopotential model (65). (B) Free-air gravity anomalies predicted by the TX2008-based mantle flow model shown in Fig. 12B. (C) Free-air gravity anomalies predicted by the S20RTS-based mantle flow model shown in Fig. 12A. (D) Free-air gravity anomalies predicted when the mantle flow calculated in (C) is modeled with a free-slip surface boundary rather than viscously coupled tectonic plates. All fields are truncated at spherical harmonic degree $\ell = 16$.

shear stress on the base of the plate. Our mantle flow modeling does not currently incorporate these additional thermomechanical processes.

If the EPR were spreading symmetrically, then it would have migrated eastward relative to the mantle-wide upwelling. Along the EPR, both asymmetric accretion and discrete ridge jumps are evident, presumably reflecting variability in the melt migration rate and spreading rate (24), and are particularly evident in the interval from about 33 Ma to 8 Ma. Fast spreading generates young, thin lithosphere above the upwelling and results in generally short interval lengths between ridge jumps, which, in the limit of high melt migration and fast spreading, would result in asymmetric accretion rather than discrete ridge jumps.

If, as our results show (Figs. 10B and 11), the deeper mantle is contributing significantly to the buoyancy flux in the vicinity of the EPR, correlated geophysical or geochemical signatures should help to further corroborate this. Geophysically, the region of high radial velocities at 650-km depth in the vicinity of Easter Island (Figs. 1 and 7B) also underlies the eastern extension of the broad South Pacific Superswell, identified as a clustering of young volcanic islands and anomalously shallow depths that are not attributable to perturbations in lithospheric thermal structure (67, 68). Careful examination of the cross section in Figs. 8B and 11 reveals that the predicted, dominantly westward asthenospheric flows have small upward components of motion, and they overlie a region of positive buoyancy that extends down to the mantle transition zone, thereby giving rise to the dynamic topography associated with the Superswell. Thus, the flow calculations are compatible with the relatively shallow source for the dynamic topography inferred in this region (69, 70), as opposed to the deep-mantle support predicted by Conrad *et al.* (47). We further suggest that anomalous isotopic compositions of the so-called South Pacific isotopic and thermal anomaly (SOPITA) volcanism (69, 70) may be related to the horizontally advected flux of deep mantle-derived material into the asthenosphere beneath the South Pacific Superswell (Fig. 8B). This implies a decoupling of the larger deep-mantle plume-like source situated to the east, closer to Easter Island, from the surface manifestations of most of the SOPITA volcanoes. Once again, this is compatible with observations from the age distributions and isotopic geochemistry of the SOPITA volcanoes (69).

CONCLUSIONS

The most significant conclusion of the present work is that there is a dynamical linkage between the longitudinal stability of the long-term (tens of millions of years) mantle-wide convective flow beneath the EPR and the kinematically reconstructed longitudinal stability in the position of the EPR over the past 50 My to 80 My. This dynamical linkage includes both the longitudinal fixity of the EPR and the marked and persistent asymmetry in the EPR spreading. We further show that, at least given existing paleo-age grid reconstructions and corresponding plate boundary evolution, the subduction-related buoyancy fluxes of the Pacific- and Farallon-related plates are uncorrelated. This lack of correlation suggests that the traditional model of plate motions mainly controlled by slab-pull forces is not a viable explanation for the relative longitudinal fixity of the EPR.

Our mantle-dynamic modeling highlights deep-mantle buoyancy under the EPR as a significant (40 to 70%) contributor to the plate driving forces in the Pacific hemisphere. The dynamical importance of deep-mantle upwellings, extracting up to 20 TW from CMB (44, 50), is compatible with recent estimates of high CMB heat flux drawn from

the core that are derived from mineral physical arguments (16, 17). High heat transport across the CMB would also account for up to approximately 50% of the heat flux at the top of the mantle (12). This emphasizes that the top-down driven convective system in which all the buoyancy driving flow that arises at the upper boundary is incompatible with the convective system modeled here, in which both upper and lower thermal boundary layers contribute about equally to the overall buoyancy fluxes. Finally, this work highlights the necessity of joint seismic-geodynamic tomography-based model inversions to derive the volumetric distribution of density anomalies that drive global mantle convective flow. Simple velocity to density scaling of tomography, as commonly carried out in geodynamics, yields significant mismatches to an array of convection-related geophysical observables. These misfits between prediction and observation thus provide a basis for discriminating among mantle flow models.

MATERIALS AND METHODS

We computed ridge migration behavior by determining the RRT for all main ocean basin spreading systems over the past 83 My. RRT is defined as the amount of time a spreading axis has occupied any given 0.5° by 0.5° grid cell as determined by rotating the present-day oceanic age grid (19) at 1-My time steps from 0 to 83 Ma (C34ny). The location of ridges at each time step was demarcated by grid cells, where the age of the oceanic lithosphere equaled the reconstruction age to within 1 My.

The subduction-related buoyancy flux analysis took the paleo-age grids of Müller *et al.* (71) as input, the corresponding plate boundaries as a function of age (72), and rotations (73) slightly edited to conform to the paleo-age grid. Note that the rotations (73) do not have their associated uncertainties, and therefore, it is not possible with these files to determine uncertainties in any of the estimated quantities below. For each age, we (i) computed the area of each plate; (ii) determined the bounding subduction zone triple junctions between the Pacific, Farallon, Nazca, Cocos, and Juan de Fuca + Vancouver plates as delineated by Gurnis *et al.* (72); and (iii) defined all the corresponding pairs of subducting versus overriding plates for each 1-My time interval from the present to 78 Ma during which each plate existed. For each of the plate pairs, the corresponding instantaneous rotation was calculated, and the effective length of each of the subduction zone segments was computed. In addition, for each plate pair, the area-weighted mean of the square root of the age of each grid cell on the subducting plate abutting the subduction boundary was computed. The area weights were based on the area represented by each of the 10th of a degree grid cells in the paleo-age grids along the plate boundary to account for area distortion associated with the rectilinear grid. Finally, the length-weighted mean subduction rate implied by the combination of triple-junction locations and instantaneous rotations (that is, rotations per 1-My interval) was computed. Additional details related to this analysis were included in the Supplementary Materials.

The global mantle flow field calculations were based on joint seismic-geodynamic tomography inversions (39, 40) that mapped the spatial distribution of density in the mantle through a simultaneous inversion of seismic travel-time and global geodynamic data (40). The analytical framework of these calculations is discussed in detail by Forte (42), Glišović *et al.* (44), Forte *et al.* (54), and Simmons *et al.* (58). Details related to the importance of establishing the viscosity structure and 3D density distribution are discussed extensively throughout the text and need not be reiterated here.

SUPPLEMENTARY MATERIALS

Supplementary material for this article is available at <http://advances.sciencemag.org/cgi/content/full/2/12/e1601107/DC1>

fig. S1. RRT in the NNR frame of reference from present to 50 Ma.
fig. S2. Data sources for ridge drift calculations.

fig. S3. Subduction-related buoyancy flux components of the Pacific and Farallon-related plates.
table S1. Rotation poles and associated covariance parameters used in our reconstructions.
table S2. Rotation poles for the major mid-ocean ridges relative to the Indo-Atlantic hot spot reference frame, listed in 5-My increments.
References (77–91)

REFERENCES AND NOTES

1. D. Forsyth, S. Uyeda, Relative importance of driving forces of plate motion. *Geophys. J. R. Astron. Soc.* **43**, 163–200 (1975).
2. F. M. Richter, Dynamical models for sea floor spreading. *Rev. Geophys. Space Phys.* **11**, 223–287 (1973).
3. F. M. Richter, On the driving mechanism of plate tectonics. *Tectonophysics* **38**, 61–88 (1977).
4. F. M. Richter, Mantle convection models. *Annu. Rev. Earth Planet. Sci.* **6**, 9–19 (1978).
5. B. A. Buffett, D. B. Rowley, Plate bending at subduction zones: Consequences for the direction of plate motions. *Earth Planet. Sci. Lett.* **245**, 359–364 (2006).
6. C. P. Conrad, B. H. Hager, Effects of plate bending and fault strength at subduction zones on plate dynamics. *J. Geophys. Res. Solid Earth* **104**, 17551–17571 (1999).
7. C. P. Conrad, C. Lithgow-Bertelli, The temporal evolution of plate driving forces: Importance of “slab suction” versus “slab pull” during the Cenozoic. *J. Geophys. Res.* **109**, B10407 (2004).
8. A. M. Forte, *Encyclopedia of Solid Earth Geophysics*, H. K. Gupta, Ed. (Springer, 2011), pp. 977–983.
9. D. L. Anderson, Top-down tectonics? *Science* **293**, 2016–2018 (2001).
10. D. Anderson, *New Theory of the Earth* (Cambridge Univ. Press, 2007), 384 pp.
11. G. F. Davies, *Dynamic Earth: Plates, Plumes and Mantle Convection* (Cambridge Univ. Press, 1999), 472 pp.
12. T. Lay, J. Hernlund, B. A. Buffett, Core–mantle boundary heat flow. *Nat. Geosci.* **1**, 25–32 (2008).
13. N. H. Sleep, Hotspots and mantle plumes: Some phenomenology. *J. Geophys. Res.* **95**, 6715–6736 (1990).
14. F. D. Stacey, P. M. Davis, *Physics of the Earth* (Cambridge Univ. Press, ed. 4, 2008), 532 pp.
15. F. D. Stacey, D. E. Loper, The thermal boundary-layer interpretation of D'' and its role as a plume source. *Phys. Earth Planet. Inter.* **33**, 45–55 (1983).
16. N. de Koker, G. Steinle-Neumann, V. Vlcek, Electrical resistivity and thermal conductivity of liquid Fe alloys at high P and T, and heat flux in Earth's core. *Proc. Natl. Acad. Sci. U.S.A.* **109**, 4070–4073 (2012).
17. M. Pozzo, C. Davies, D. Gubbins, D. Alfè, Thermal and electrical conductivity of iron at Earth's core conditions. *Nature* **485**, 355–358 (2012).
18. S. Stein, H. J. Melosh, J. B. Minster, Ridge migration and asymmetric sea-floor spreading. *Earth Planet. Sci. Lett.* **36**, 51–66 (1977).
19. R. D. Müller, M. Sdrolias, C. Gaina, W. R. Roest, Age, spreading rates, and spreading asymmetry of the world's ocean crust. *Geochim. Geophys. Geosyst.* **9**, Q04006 (2008).
20. S. C. Cande, D. Kent, Revised calibration of the geomagnetic polarity timescale for the late Cretaceous and Cenozoic. *J. Geophys. Res. Solid Earth* **100**, 6093–6095 (1995).
21. C. O'Neill, R. Müller, B. Steinberger, On the uncertainties in hot spot reconstructions and the significance of moving hot spot reference frames. *Geochim. Geophys. Geosyst.* **6**, Q04003 (2005).
22. P. Wessel, L. W. Kroenke, Pacific absolute plate motion since 145 Ma: An assessment of the fixed hot spot hypothesis. *J. Geophys. Res.* **113**, B06101 (2008).
23. T. Chang, Estimating the relative rotation of two tectonic plates from boundary crossings. *J. Am. Stat. Assoc.* **83**, 178–183 (1988).
24. C. J. Rowan, D. B. Rowley, Spreading behaviour of the Pacific-Farallon ridge system since 83 Ma. *Geophys. J. Int.* **197**, 1273–1283 (2014).
25. R. Granot, S. C. Cande, J. M. Stock, D. Damaske, Revised Eocene-Oligocene kinematics for the West Antarctic rift system. *Geophys. Res. Lett.* **40**, 279–284 (2013).
26. R. Sutherland, The significance of Antarctica for studies of global geodynamics, in *Antarctica: A Keystone in a Changing World*, A. K. Cooper, P. J. Barrett, H. Stagg, B. Storey, E. Stump, W. Wise, 10th ISAES Editorial Team, Eds. (National Academies Press, 2008), pp. 115–124.
27. B. Steinberger, R. Sutherland, R. O'Connell, Prediction of Emperor-Hawaii seamount locations from a revised model of global plate motion and mantle flow. *Nature* **430**, 167–173 (2004).
28. M. B. Croon, S. C. Cande, J. M. Stock, Revised Pacific-Antarctic plate motions and geophysics of the Menard Fracture Zone. *Geochim. Geophys. Geosyst.* **9**, Q07001 (2008).
29. S. C. Cande, C. Raymond, J. Stock, W. Haxby, Geophysics of the Pitman Fracture-Zone and Pacific-Antarctic plate motions during the Cenozoic. *Science* **270**, 947–953 (1995).
30. W. R. Keller, “Cenozoic plate tectonic reconstructions and plate boundary processes in the Southwest Pacific,” thesis, California Institute of Technology (2004).
31. C. Gaina, D. R. Müller, J.-Y. Royer, J. Stock, J. Hardebeck, P. Symonds, The tectonic history of the Tasman Sea: A puzzle with 13 pieces. *J. Geophys. Res.* **103**, 12413–12433 (1998).
32. P. Molnar, T. Atwater, J. Hammerickx, S. M. Smith, Magnetic anomalies, bathymetry, and tectonic evolution of the South Pacific since the Late Cretaceous. *Geophys. J. R. Astron. Soc.* **49**, 383–420 (1975).
33. J. M. O'Connor, R. A. Duncan, Evolution of the Walvis Ridge-Rio Grande rise hot spot system: Implications for African and South American plate motions over plumes. *J. Geophys. Res.* **95**, 17475–17502 (1990).
34. C. DeMets, R. G. Gordon, D. F. Argus, Geologically current plate motions. *Geophys. J. Int.* **181**, 1–80 (2010).
35. J.-Y. Royer, T. Chang, Evidence for relative motions between the Indian and Australian plates during the last 20 m.y. from plate tectonic reconstructions: Implications for the deformation of the Indo-Australian plate. *J. Geophys. Res.* **96**, 11779–11802 (1991).
36. S. C. Cande, W. F. Haxby, Eocene propagating rifts in the southwest Pacific and their conjugate features on the Nazca plate. *J. Geophys. Res.* **96**, 19609–19622 (1991).
37. D. L. Turcotte, G. Schubert, *Geodynamics* (Cambridge Univ. Press, ed. 2, 2002).
38. S. C. Solomon, N. H. Sleep, R. M. Richardson, On the forces driving plate tectonics: Inferences from absolute plate velocities and intraplate stress. *Geophys. J. Int.* **42**, 769–801 (1975).
39. A. M. Forte, S. Quéré, R. Moucha, N. A. Simmons, S. P. Grand, J. X. Mitrovica, D. B. Rowley, Joint seismic–geodynamic–mineral physical modelling of African geodynamics: A reconciliation of deep-mantle convection with surface geophysical constraints. *Earth Planet. Sci. Lett.* **295**, 329–341 (2010).
40. N. A. Simmons, A. M. Forte, S. P. Grand, Joint seismic, geodynamic and mineral physical constraints on three-dimensional mantle heterogeneity: Implications for the relative importance of thermal versus compositional heterogeneity. *Geophys. J. Int.* **177**, 1284–1304 (2009).
41. J. X. Mitrovica, A. M. Forte, A new inference of mantle viscosity based upon joint inversion of convection and glacial isostatic adjustment data. *Earth Planet. Sci. Lett.* **225**, 177–189 (2004).
42. A. M. Forte, *Treatise on Geophysics*, G. Schubert, Ed. (Elsevier, 2007), pp. 805–858.
43. B. H. Hager, R. J. O'Connell, A simple global model of plate dynamics and mantle convection. *J. Geophys. Res.* **86**, 4843–4867 (1981).
44. P. Glišović, A. M. Forte, R. Moucha, Time-dependent convection models of mantle thermal structure constrained by seismic tomography and geodynamics: Implications for mantle plume dynamics and CMB heat flux. *Geophys. J. Int.* **190**, 785–815 (2012).
45. M. D. Behn, C. P. Conrad, P. G. Silver, Detection of upper mantle flow associated with the African superplume. *Earth Planet. Sci. Lett.* **224**, 259–274 (2004).
46. C. P. Conrad, M. D. Behn, Constraints on lithosphere net rotation and asthenospheric viscosity from global mantle flow models and seismic anisotropy. *Geochem. Geophys. Geosyst.* **11**, Q05W05 (2010).
47. C. P. Conrad, T. A. Bianco, E. I. Smith, P. Wessel, Patterns of intraplate volcanism controlled by asthenospheric shear. *Nat. Geosci.* **4**, 317–321 (2011).
48. C. DeMets, R. G. Gordon, D. F. Argus, S. Stein, Effect of recent revisions to the geomagnetic reversal time scale on estimates of current plate motions. *Geophys. Res. Lett.* **21**, 2191–2194 (1994).
49. T. Hoinaki, A. M. Jellinek, A. Lenardic, Viscous coupling at the lithosphere–asthenosphere boundary. *Geochem. Geophys. Geosyst.* **12**, Q0AK02 (2011).
50. P. Glišović, A. M. Forte, Importance of initial buoyancy field on evolution of mantle thermal structure: Implications of surface boundary conditions. *Geosci. Front.* **6**, 3–22 (2015).
51. P. Glišović, A. M. Forte, Reconstructing the Cenozoic evolution of the mantle: Implications for mantle plume dynamics under the Pacific and Indian plates. *Earth Planet. Sci. Lett.* **390**, 146–156 (2014).
52. J. Ritsema, H. J. van Heijst, J. H. Woodhouse, Complex shear velocity structure imaged beneath Africa and Iceland. *Science* **286**, 1925–1928 (1999).
53. J. Ritsema, H. J. van Heijst, J. H. Woodhouse, Global transition zone tomography. *J. Geophys. Res.* **109**, B02302 (2004).
54. A. M. Forte, N. A. Simmons, S. P. Grand, *Treatise of Geophysics*, G. Schubert, Ed. (Elsevier, 2014).
55. R. Moucha, A. M. Forte, Changes in African topography driven by mantle convection. *Nat. Geosci.* **4**, 707–712 (2011).
56. R. Moucha, A. M. Forte, D. B. Rowley, J. X. Mitrovica, N. A. Simmons, S. P. Grand, Deep mantle forces and the uplift of the Colorado Plateau. *Geophys. Res. Lett.* **36**, L19310 (2009).
57. D. B. Rowley, A. M. Forte, R. Moucha, J. X. Mitrovica, N. A. Simmons, S. P. Grand, Dynamic topography change of the eastern United States since 3 million years ago. *Science* **340**, 1560–1563 (2013).
58. N. A. Simmons, A. M. Forte, L. Boschi, S. P. Grand, GyPSuM: A joint tomographic model of mantle density and seismic wave speeds. *J. Geophys. Res. Solid Earth* **115**, B12310 (2010).

59. Y. J. Gu, A. L. Lerner-Lam, A. M. Dziewonski, G. Ekström, Deep structure and seismic anisotropy beneath the East Pacific Rise. *Earth Planet. Sci. Lett.* **232**, 259–272 (2005).

60. B. Kustowski, G. Ekstrom, A. M. Dziewonski, Anisotropic shear-wave velocity structure of the Earth's mantle: A global model. *J. Geophys. Res.* **113**, B06306 (2008).

61. R. Moucha, A. M. Forte, J. X. Mitrovica, D. B. Rowley, S. Quéré, N. A. Simmons, S. P. Grand, Dynamic topography and long-term sea-level variations: There is no such thing as a stable continental platform. *Earth Planet. Sci. Lett.* **271**, 101–108 (2008).

62. B. S. A. Schubert, H.-P. Bunge, J. Ritsema, Tomographic filtering of high-resolution mantle circulation models: Can seismic heterogeneity be explained by temperature alone? *Geochem. Geophys. Geosyst.* **10**, Q05W03 (2009).

63. A. Ghosh, W. E. Holt, Plate motions and stresses from global dynamic models. *Science* **335**, 838–843 (2012).

64. A. K. McNamara, S. Zhong, Thermochemical structures beneath Africa and the Pacific Ocean. *Nature* **437**, 1136–1139 (2005).

65. B. Tapley, J. Ries, S. Bettadpur, D. Chambers, M. Cheng, F. Condi, S. Poole, The GGM03 mean Earth gravity model from GRACE. *EOS Trans. Am. Geophys. Union* **88**, G42A-03 (2007).

66. E. Mittelstaedt, G. Ito, J. van Hunen, Repeat ridge jumps associated with plume-ridge interaction, melt transport, and ridge migration. *J. Geophys. Res.* **114**, 1–20 (2011).

67. M. K. McNutt, Superswells. *Rev. Geophys.* **36**, 211 (1998).

68. L. Sichoix, A. Bonneville, M. K. McNutt, The seafloor swells and Superswell in French Polynesia. *J. Geophys. Res.* **103**, 27123–27133 (1998).

69. A. A. P. Koppers, Short-lived and discontinuous intraplate volcanism in the South Pacific: Hot spots or extensional volcanism? *Geochem. Geophys. Geosyst.* **4**, 1089 (2003).

70. H. Staudigel, K.-H. Park, M. Pringle, J. L. Rubenstone, W. H. F. Smith, A. Zindler, The longevity of the South Pacific isotopic and thermal anomaly. *Earth Planet. Sci. Lett.* **102**, 24–44 (1991).

71. R. D. Müller, M. Sdrolias, C. Gaina, B. Steinberger, C. Heine, Long-term sea-level fluctuations driven by ocean basin dynamics. *Science* **319**, 1357–1362 (2008).

72. M. Gurnis, M. Turner, S. Zahirovic, L. DiCaprio, S. Spasojevic, R. Dietmar Müller, J. Boyden, M. Seton, V. Constantin Manea, D. J. Bower, Plate tectonic reconstructions with continuously closing plates. *Comput. Geosci.* **38**, 35–42 (2012).

73. M. Seton, R. D. Müller, S. Zahirovic, C. Gaina, T. Torsvik, G. Shephard, A. Talsma, M. Gurnis, M. Turner, S. Maus, M. Chandler, Global continental and ocean basin reconstructions since 200 Ma. *Earth Sci. Rev.* **113**, 212–270 (2012).

74. P. Wessel, W. H. F. Smith, New improved version of generic mapping tools released. *EOS Trans. Am. Geophys. Union* **79**, 579 (1998).

75. P. Bird, An updated digital model of plate boundaries. *Geochem. Geophys. Geosyst.* **4**, 1027 (2003).

76. P. M. Mathews, T. A. Herring, B. A. Buffett, Modeling of nutation and precession: New nutation series for nonrigid Earth and insights into the Earth's interior. *J. Geophys. Res.* **107**, 2068 (2002).

77. R. D. Müller, J.-Y. Royer, S. C. Cande, W. R. Roest, S. Maschenko, New constraints on the Late Cretaceous/Tertiary plate tectonic evolution of the Caribbean, in *Caribbean Basins*, P. Mann, Ed. (Elsevier, 1999), pp. 33–59.

78. S. Merkouriev, C. DeMets, A high-resolution model for Eurasia-North America plate kinematics since 20 Ma. *Geophys. J. Int.* **173**, 1064–1083 (2008).

79. C. Gaina, W. R. Roest, R. Müller, Late Cretaceous–Cenozoic deformation of northeast Asia. *Earth Planet. Sci. Lett.* **197**, 273–286 (2002).

80. B. C. Horner-Johnson, R. G. Gordon, S. M. Cowles, D. F. Argus, The angular velocity of Nubia relative to Somalia and the location of the Nubia-Somalia-Antarctica triple junction. *Geophys. J. Int.* **162**, 221–238 (2005).

81. J. M. Bull, C. DeMets, K. S. Krishna, D. J. Sanderson, S. Merkouriev, Reconciling plate kinematic and seismic estimates of lithospheric convergence in the central Indian Ocean. *Geology* **38**, 307–310 (2010).

82. S. C. Cande, P. Patriat, J. Dymnt, Motion between the Indian, Antarctic and African plates in the early Cenozoic. *Geophys. J. Int.* **183**, 127–149 (2010).

83. P. Molnar, F. Pardo-Casas, J. Stock, The Cenozoic and Late Cretaceous evolution of the Indian Ocean basin: Uncertainties in the reconstructed positions of the Indian, African, and Antarctic plates. *Basin Res.* **1**, 23–40 (1988).

84. J. Lemaux II, R. G. Gordon, J.-Y. Royer, Location of the Nubia-Somalia boundary along the Southwest Indian Ridge. *Geology* **30**, 339–342 (2002).

85. P. Patriat, H. Sloan, D. Sauter, From slow to ultraslow: A previously undetected event at the Southwest Indian Ridge at ca. 24 Ma. *Geology* **36**, 207–210 (2008).

86. A. Bernard, M. Munschy, Y. Rotstein, D. Sauter, Refined spreading history at the Southwest Indian Ridge for the last 96 Ma, with the aid of satellite gravity data. *Geophys. J. Int.* **162**, 765–778 (2005).

87. S. C. Cande, J. M. Stock, Pacific–Antarctic–Australia motion and the formation of the Macquarie Plate. *Geophys. J. Int.* **157**, 399–414 (2004).

88. J. M. Whittaker, R. D. Müller, G. Leitchenkov, H. Stagg, M. Sdrolias, C. Gaina, A. Goncharov, Major Australian–Antarctic plate reorganization at Hawaiian–Emperor bend time. *Science* **318**, 83–86 (2007).

89. S. Cande, J. Stock, *The Cenozoic Southern Ocean: Tectonics, Sedimentation, and Climate Change Between Australia and Antarctica*, N. F. Exon, J. P. Kennett, M. J. Malone, Eds. (American Geophysical Union, 2004), pp. 5–18.

90. R. D. Larter, A. P. Cunningham, P. F. Barker, K. Gohl, F. O. Nitsche, Tectonic evolution of the Pacific margin of Antarctica 1. Late Cretaceous tectonic reconstructions. *J. Geophys. Res. Solid Earth* **107**, EPM 5–1–EPM 5–19 (2002).

91. D. Wilder, "Relative motion history of the Pacific–Nazca (Farallon) plates since 30 million years ago," thesis, University of South Florida (2003).

Acknowledgments: Calculations and various figures used GMT (Generic Mapping Tools) from Wessel and Smith (74). We thank P. Doubrovine for sharing his code for computing interpolated rotations with uncertainties. **Funding:** D.B.R. and A.M.F. thank the Canadian Institute for Advanced Research–Earth System Evolution Program for postdoctoral fellowship support to C.J.R. and members of Engaging Scientists and Engineers in Policy for discussions and encouragement. A.M.F. acknowledges funding from the Canadian Institute for Advanced Research, the Natural Sciences and Engineering Research Council of Canada, the John Simon Guggenheim Memorial Foundation, and the University of Florida. Work performed by N.A.S. is under the auspices of the U.S. Department of Energy under contract DE-AC52-07NA27344. S.P.G. acknowledges NSF grant EAR0309189. **Author contributions:** D.B.R. and A.M.F. recognized the large-scale patterns. D.B.R. and A.M.F. were primarily responsible for writing the paper, with contributions from all others. D.B.R. and C.J.R. performed the EPR kinematic analysis. D.B.R. performed the subduction zone buoyancy flux proxy calculations. A.M.F. did the mantle dynamic calculations with contributions from P.G. and R.M. S.P.G. and N.A.S. collected the seismic tomography data. N.A.S., S.P.G., and A.M.F. performed the joint seismic-geodynamic inversions. **Competing interests:** The authors declare that they have no competing interests. **Data and materials availability:** All data needed to evaluate the conclusions in the paper are present in the paper and/or the Supplementary Materials. Additional data related to this paper may be requested from the authors.

Submitted 16 May 2016

Accepted 21 November 2016

Published 23 December 2016

10.1126/sciadv.1601107

Citation: D. B. Rowley, A. M. Forte, C. J. Rowan, P. Glišović, R. Moucha, S. P. Grand, N. A. Simmons, Kinematics and dynamics of the East Pacific Rise linked to a stable, deep-mantle upwelling. *Sci. Adv.* **2**, e1601107 (2016).

This article is published under a Creative Commons license. The specific license under which this article is published is noted on the first page.

For articles published under [CC BY](#) licenses, you may freely distribute, adapt, or reuse the article, including for commercial purposes, provided you give proper attribution.

For articles published under [CC BY-NC](#) licenses, you may distribute, adapt, or reuse the article for non-commercial purposes. Commercial use requires prior permission from the American Association for the Advancement of Science (AAAS). You may request permission by clicking [here](#).

The following resources related to this article are available online at <http://advances.sciencemag.org>. (This information is current as of March 3, 2017):

Updated information and services, including high-resolution figures, can be found in the online version of this article at:

<http://advances.sciencemag.org/content/2/12/e1601107.full>

Supporting Online Material can be found at:

<http://advances.sciencemag.org/content/suppl/2016/12/19/2.12.e1601107.DC1>

This article **cites 79 articles**, 20 of which you can access for free at:

<http://advances.sciencemag.org/content/2/12/e1601107#BIBL>